

VARIABLE THERMAL RESISTOR BASED ON COMPRESSIBLE FOAMS

by

Weizhi Liao

A Thesis

Submitted to the Faculty of Purdue University

In Partial Fulfillment of the Requirements for the degree of

Master of Science in Mechanical Engineering



School of Mechanical Engineering

West Lafayette, Indiana

August 2020

THE PURDUE UNIVERSITY GRADUATE SCHOOL
STATEMENT OF COMMITTEE APPROVAL

Dr. Xiulin Ruan, Co-Chair

School of Mechanical Engineering

Dr. Amy Marconnet, Co-Chair

School of Mechanical Engineering

Dr. Liang Pan

School of Mechanical Engineering

Approved by:

Dr. Nicole L. Key

ACKNOWLEDGMENTS

It is my honor to express my deep gratitude to everyone who helped and guided me for the past two years.

First of all, I am very grateful to my co-advisors, Profs. Xiulin Ruan and Amy Marconnet, for providing me the opportunity to conduct research and work in such talented research groups. Prof. Ruan has been a supportive mentor who not only provides guidance in academics, but also creates a positive and encouraging environment for me to study and learn. Prof. Marconnet has provided a lot of support and guidance on conducting experiments throughout this thesis.

I also want to thank my committee member, Prof. Liang Pan, for his support and insights bringing into this thesis.

Besides, I want to thank especially Dr. Tingting Du, who guided me all around from the first day of my research. I want to thank Joseph Peoples for helping me on both experiments and simulations, and Zixin Xiong for the support on performing simulations. I also want to thank Rajath Kantharaj for the training on using the infrared microscope.

It is unfortunate that I could not mention everyone who helped and supported me. But I want to thank all of the people who enriched my experience and brought many wonderful moments to me over the past two years here at Purdue University.

TABLE OF CONTENTS

LIST OF TABLES	6
LIST OF FIGURES	7
ABSTRACT.....	10
1. INTRODUCTION	11
1.1 Performance Metrics	12
1.2 Past Work on Thermal Switches and Thermal Regulators	13
1.3 Thermal Regulators with Compressible Foams	15
1.4 Overview of This Work	16
2. SYSTEM TESTING WITH GRAPHENE/PDMS FLEXIBLE FOAM.....	18
2.1 Design of the Experimental Apparatus	19
2.1.1 System Modeling and Analysis	19
2.1.2 Experimental Setup Design Concepts and Expectations	20
2.1.3 Actual Experiment Setup	22
2.2 Testing and Results	23
2.2.1 Testing under Ambient Temperature	24
2.2.2 Testing in Environmental Chamber	28
2.3 Reliability and Cycling Test	32
2.4 Discussions and Conclusion	34
3. VARIABLE THERMAL CONDUCTIVITY AND CONDUCTANCE OF COMPRESSIBLE POLYMER FOAM.....	35
3.1 Experimental Setup and Method.....	35
3.2 Assumptions and Determination of Analysis Methods	37
3.3 Experiment Results and Analysis	40
3.3.1 Compressed State.....	41
3.3.2 Uncompressed State: Near-Interface Approximation.....	42
3.3.3 Uncompressed State: One-Dimensional Fin Equation	45
3.3.4 Uncompressed State: 3-D Numerical Simulation.....	47
3.4 Results Discussion and the Spring Model	51
4. SIMULATION OF COMPRESSIBLE GRAPHENE NANOFOAM	54

4.1	Simulation Method.....	54
4.2	Simulation Process and Results	55
4.3	Simulation Outcomes and Discussion	59
5.	CONCLUSION AND FUTURE WORK	60
	APPENDIX A. EXTRA ITERATION STEPS IN COMSOL SIMULATION	61
	APPENDIX B. GRPAHENE NANOFOAM MODEL	63
	REFERENCES	64

LIST OF TABLES

Table 1.1. Examples of thermal switches and thermal regulators.	14
Table 1.2. Empirical formulas for effective thermal conductivity of porous media.....	15
Table 3.1. Power Source Voltage, Temperature Gradients, and Heat Flux for the <i>Compressed</i> Packing Foam Experiment.....	41
Table 3.2. Temperature Gradients and Heat Flux for the <i>Uncompressed</i> Packing Foam Analysis by Near-Interface Approximation.....	44
Table 3.3. Best fit values of the fin parameter m extracted with one-dimensional fin equation. .	46
Table 3.4. Mean Squared Error of Simulated Result with the Prescribed Temperature Boundary Condition on the Cold Side. The best-fit value is bolded and in red text.	50
Table 3.5. Mean Squared Error of Simulated Result with the Prescribed Heat Flux Boundary Condition on the Cold Side. The best-fit value is bolded and in red text.	50
Table 3.6. Best fit thermal conductivity and convective heat transfer coefficient for the compressed sample with different fitting methods. The resulting MSE is shown for the COMSOL fitting approach.	51
Table 4.1. Graphene Nanofoam Simulation Time Period.....	55
Table A.1. Second Round of Iteration: Mean Squared Error of Simulated Result with the Prescribed Temperature Boundary Condition on the Cold Side.....	61
Table A.2. Third and Final Round of Iteration: Mean Squared Error of Simulated Result with the Prescribed Temperature Boundary Condition on the Cold Side.....	61
Table A.3. Third and Final Round of Iteration: Mean Squared Error of Simulated Result with the Prescribed Heat Flux Boundary Condition on the Cold Side.	61
Table A.4. Third and Final Round of Iteration: Mean Squared Error of Simulated Result with the Prescribed Heat Flux Boundary Condition on the Cold Side.	62

LIST OF FIGURES

Figure 1.1. Predicted effective thermal conductivity as a function of porosity for (a) $K_{solid} = 5$ W/(m-K) and $K_{fluid} = 1$ W/(m-K) and (b) $K_{solid} = 1$ W/(m-K) and $K_{fluid} = 5$ W/(m-K) based on the models from Ref. 21-23.	16
Figure 2.1. SEM images of the porous graphene foam.....	18
Figure 2.2. Schematic Diagram and thermal circuit of the simplified system.....	19
Figure 2.3. CAD model of the system testing design concept.....	21
Figure 2.4. Actual experimental setup with power supply and data logger.....	22
Figure 2.5. A closer look at the core section of the experimental setup, as only the fanned heat sink and the graphene foam are exposed to ambient air. The aluminum bar and the input heat source are insulated by packing foam.	22
Figure 2.6. The device temperature with respect to foam thickness at various input heat flux under room temperature.	24
Figure 2.7. The fin temperature with respect to foam thickness at various input heat flux under room temperature.	25
Figure 2.8. The temperature difference across the graphene foam with respect to foam thickness under room temperature.	26
Figure 2.9. The temperature difference across the graphene foam with respect to input heat flux under room temperature.	26
Figure 2.10. Calculated thermal resistance as functions of foam thickness at each input heat flux level under room temperature.	27
Figure 2.11. A contour plot showing how foam thickness and input heat flux affect the resultant device temperature under room temperature.	28
Figure 2.12. The device temperature with respect to the ambient temperature at each thickness level in the environmental chamber.	29
Figure 2.13. The fin temperature with respect ambient temperature at each thickness level in the environmental chamber.....	30
Figure 2.14. The temperature difference across the graphene foam with respect to ambient temperature in the environmental chamber.....	30
Figure 2.15. Thermal resistance of the graphene foam as functions of foam thickness at each input heat flux level.....	31
Figure 2.16. A contour plot showing how foam thickness and input heat flux affect the resultant device temperature in the chamber.	32
Figure 2.17. Temperature measurements for the reliability test of the graphene foam.	33

Figure 3.1. (Left) Schematic and (Right) photograph of the experiment setup for the miniaturized reference bar method with temperature measurements obtained with an infrared (IR) microscope.	36
Figure 3.3. Example temperature map showing the temperature distribution of the sandwich structure at the <i>compressed</i> state, with the white box indicating the selected region for analysis. Each pixel is approximately 12 μm	38
Figure 3.4. Example temperature map showing the temperature distribution of the sandwich structure at the <i>uncompressed</i> state, with the white box indicating the selected region for analysis. Each pixel is approximately 12 μm	38
Figure 3.5. Example temperature profile along the heat flow direction for the <i>compressed</i> state.	39
Figure 3.6. Example temperature profile along the heat flow direction for the <i>uncompressed</i> state.	39
Figure 3.7. Heat flux through the sample in the <i>compressed</i> state as a function of the sample temperature gradient. The red dashed line shows the best fit (with fixed y-intercept), the slope of which is the effective thermal conductivity of compressed packing foam.	42
Figure 3.8. Moving average of local temperature gradient for near-interface analysis with different sample windows for the derivatives.	43
Figure 3.9. Heat flux through the sample in the <i>uncompressed</i> state as a function of the sample temperature gradient near the reference-sample interface. The red dashed line shows the best fit (with fixed y-intercept), the slope of which is the effective thermal conductivity of <i>uncompressed</i> packing foam using near-interface approximation.	44
Figure 3.10. Normalized temperature profile obtained from thermal imaging (blue points) compared to the best-fit one-dimensional fin equation (red dashed line).	46
Figure 3.11. Proportional fitting for the derivation of the effective convective heat transfer coefficient of uncompressed packing foam using fin equation model.	47
Figure 3.12. Geometry and surface temperature (in K) with a heat transfer coefficient of $h_{\text{eff}} = 0.187 \text{ W}/(\text{m}^2\text{K})$ and $k_{\text{eff}} = 0.00117 \text{ W}/(\text{m-K})$	48
Figure 3.13. Original and reduced temperature map for comparison with the COMSOL Multiphysics® simulation output.	49
Figure 3.14. Simulated Temperature Maps with two sets of boundary conditions.	49
Figure 3.15. Geometry of a spring with compression to explain the unusual thermal conductivity behavior observed for the foams.	52
Figure 4.1. The compression process of the graphene nanofoam. (Left) Uncompressed graphene nanofoam after relaxation and, (Right) Compressed graphene nanofoam before relaxation.	56
Figure 4.2. Monitoring temperature and pressure changes during sample trial of the simulation.	56

Figure 4.4. Calculated thermal conductivity converges at the end of the simulation.	58
Figure 4.5. Final calculated thermal conductivities of graphene nanofoam by MD simulation...	59
Figure B.1. Construction of Graphene Nanofoam.	63

ABSTRACT

With the world's increasing usage of electronic devices such as mobile devices and batteries, improving the reliability and performance of these devices has become more and more important. Besides the common overheating issues, low-temperature environments can also cause performance degradation or failure to these devices. Research on thermal switches and thermal regulators aims to improve the thermal management of electronic devices across a range of operating conditions. However, continuous tuning of thermal transport with all-solid-state systems is still challenging. The primary purpose of this work is to propose and demonstrate compressible foams as novel variable thermal resistors and thermal regulators to control device temperature under various input heat flux and ambient temperature. The graphene/PDMS foam is first tested in this work to demonstrate promising performance as a thermal regulator, with continuous tuning capability and a system switching ratio over ~ 4 . Then, the dependence of the thermal conductivity of polymer foams during compression is studied, where the thermal conductivity is measured using a customized system based on an infrared microscope. Unexpectedly, the thermal conductivity decreases slightly at a compression level of more than 10x, in contrast to common theories that the thermal conductivity would increase with the mass density. A simple "spring model" is proposed as a limit where the ligaments do not build contacts during compression. Our results now fall in between the "spring model" and other common theories and can be explained. To gain further insights, a molecular dynamic simulation is performed on a graphene random nanofoam on the nanoscale. The result also shows that the effective thermal conductivity along the compression direction is not sensitive to the mass density, consistent with our experimental data on the macroscopic scale. This work provides useful insights into dynamic thermal management of electronic devices.

1. INTRODUCTION

With the rapid advancement of technology, modern electronic devices are essential to the world's daily operations [1]. This increase in demand for electronic devices is requiring more efficient batteries to operate reliably at various temperature conditions [2, 3]. Lithium-ion batteries operate most effectively within a specific temperature range. Extreme temperatures hinder optimal performance (*e.g.*, reduces the driving range of electric vehicles) and also cause permanent degradation to the lifespan of the battery. Under varying operating conditions, it is beneficial to implement effective thermal regulation techniques: highly thermally conductive pathways to enable sufficient heat dissipation, as well as thermal insulation to prevent thermal runaway or to insulate the cell from a cold environment [4]. Researchers have been developing several thermal regulation techniques to ensure optimal operating conditions for batteries utilizing the concepts of thermal diodes, thermal regulators, and thermal switches. Among these, thermal switches and thermal regulators usually serve the purpose of controlling and maintaining the critical temperature of a device to allow safe and efficient operations [5].

The concept of thermal switches utilizes non-thermal mechanisms to achieve maximum or minimum thermal conductance. Gas-gap thermal switch is a simple practical solution that is adapted to many thermal-related applications, where the maximum thermal conductance ("ON" state) is achieved by physical contacts of heat conductive components and the minimum thermal conductance ("OFF" state) is achieved by disconnecting the components and filling gas as the insulator [6].

Thermal switches offer thermal control between two extreme thermal conditions. However, many applications may have more strict temperature restrictions and require continuous thermal control methods. Thermal regulators have non-linear responses that allow dynamic and continuous control to maintain the device within the desired temperature. In many cases, thermal regulators are preferred over thermal switches as maintaining critical temperature range helps improve the operating stability and performance of the system [5].

Thermal switches and thermal regulators have expanded in micro- and nano-scale applications. For example, the geometry of carbon nanostructure impacts its thermal conductivity [7, 8, 9] and thermal switches can be developed from carbon-based materials. Graphene has

outstandingly high thermal conductivity: experimental results have shown that single layer graphene (SLG) has a thermal conductivity on the order of 5,000 W/(m-K) [10], while a single carbon nanotube (CNT) on the order of 1,750 W/(m-K) at room temperature [9]. In terms of thermal switching, nanofoams consisting of graphene have been predicted to achieve switchable thermal conductivity by mechanical control of the nanofoam structure. Specifically, expanding the foam structure reduces the thermal conductivity predicted with Molecular Dynamics (MD) simulations [11].

1.1 Performance Metrics

Thermal switches and thermal regulators are solutions to maintain certain device temperatures under various levels of heat input and surrounding conditions. Thermal switches alternate between the ON and OFF states to keep devices within an acceptable temperature range, while thermal regulators keep devices within the desired temperature range with continuous thermal response.

The heat flow, Q , by conduction through an arbitrary thermal device can be calculated from the difference in the hot and cold side temperatures (T_H and T_C , respectively) using Fourier's Law assuming one-dimensional heat transfer as [12]:

$$Q = kA \frac{T_H - T_C}{L}, \quad (1.1)$$

where, k is the effective thermal conductivity of the device, A is the effective heat conduction area, and L is the effective heat transfer path length. Assuming the thermal device is hotter than its surroundings or the heat sink, T_H is the device temperature and T_C is the surrounding or heat sink temperature.

In a thermal system, thermal conductance, G , is often used as the performance metric and is defined as:

$$G = \frac{k}{L} = \frac{Q''}{T_H - T_C}, \quad (1.2)$$

where, $Q'' = Q/A$ is the heat flux through the device.

One conventional way to describe the performance metric of a thermal switch is the switching ratio, which is defined as: [13]

$$r = \frac{G_{on}}{G_{off}} = \frac{Q''_{on}/\Delta T_{on}}{Q''_{off}/\Delta T_{off}}, \quad (1.3)$$

where, $\Delta T = T_H - T_C$ is the temperature difference across the device and the subscripts “on” and “off” indicate the state.

1.2 Past Work on Thermal Switches and Thermal Regulators

A variety of thermal switches and thermal regulators have been studied across length scales and leveraging different mechanisms to adapt to specific types of applications. Table 1.1 summarizes the switching mechanism, materials, and switching ratio of various thermal switches and regulators in literature.

Table 1.1. Examples of thermal switches and thermal regulators.

Switching Mechanism	Materials	Switching Ratio, r	Ref.
Gas-gap (25 μ m)	Hg micro-droplet, air	8-60	[14]
	Si solid, air	1.6-3.0	
Gas-gap (100 μ m)	Hg micro-droplet, air	24-74	
	Si solid, air	3.6-8.0	
Thermoelectric effects	Thermoelectric modules	>100	[13]
Liquid metal droplets	Liquid metal, NaOH	~2	[15]
Liquid bridge	Deionized water	~1.5	[16]
Liquid metal droplet	Galinstan, wet	8.1-15.6	[17]
	Dry	27.4-71.3	
Liquid-solid phase transitions	Graphite/hexadecane suspensions	~3	[18]
Thermoelectric generation	Thermoelectric modules	~1.2	[19]
Thermal expansion	CNT	~5	[7]

1.3 Thermal Regulators with Compressible Foams

Foam-based structures are porous media that exhibit unique thermal characteristics. Heat transfer process in porous media depends both on the thermal conductivity of the material and its complex structure [20]. The structure is determined by the manufacturing of the media and is often complex and random. The highly porous nature of compressible foams allows physical deformations of its structure, which, in turn, alters its thermal conductivity [20]. This change in thermal conductivity with compression makes compressible foams a potential candidate for thermal switch and thermal regulator applications.

Table 1.2. Empirical formulas for the effective thermal conductivity of porous media.

Model No.	Empirical formula	Ref.
1	$K_{eff} = K_{fluid}^\varepsilon K_{solid}^{(1-\varepsilon)}$	[21]
2	$K_{eff} = K_{fluid} \left(\frac{K_{fluid}}{K_{solid}} \right)^{\left(-0.280 + 0.757 \log_{10} \varepsilon - 0.057 \log_{10} \left(\frac{K_{fluid}}{K_{solid}} \right) \right)}$	[22]
3	$K_{eff} = K_{solid} \left[\frac{3K_{fluid} + 2(1 - \varepsilon)(K_{solid} - K_{fluid})}{(2 + \varepsilon)K_{solid} + K_{fluid}(1 - \varepsilon)} \right]$	[23]

Due to the complexity of transport in non-uniform porous media, models for the thermal conductivity of these are mostly empirical or based on numerical simulations.

Table 1.2 summaries three different models and Figure 1.1 illustrates the relationship between the effective thermal conductivity of the media (K_{eff}) and the porosity of the foam (ε) and the thermal conductivity of the fluid and solid (K_{fluid} and K_{solid} , respectively). These empirical models are developed under specific experimental conditions and none of them can reliably predict all transport phenomena in porous media. For instance, the models only consider uniform samples and neglect some influential parameters such as pore size or pore distribution [20]. As shown in Figure 1.1, if $K_{solid} > K_{fluid}$, the effective thermal conductivity decreases as

porosity increases, while if $K_{solid} < K_{fluid}$, the effective thermal conductivity increases with porosity. For a compressible foam, the working fluid is air and the solid material is polymer or polymer composite. Since the porosity will decrease as the foam become compressed, existing models have predicted that the effective thermal conductivity will increase and therefore, making compressible foam a promising candidate for thermal switching mechanism.

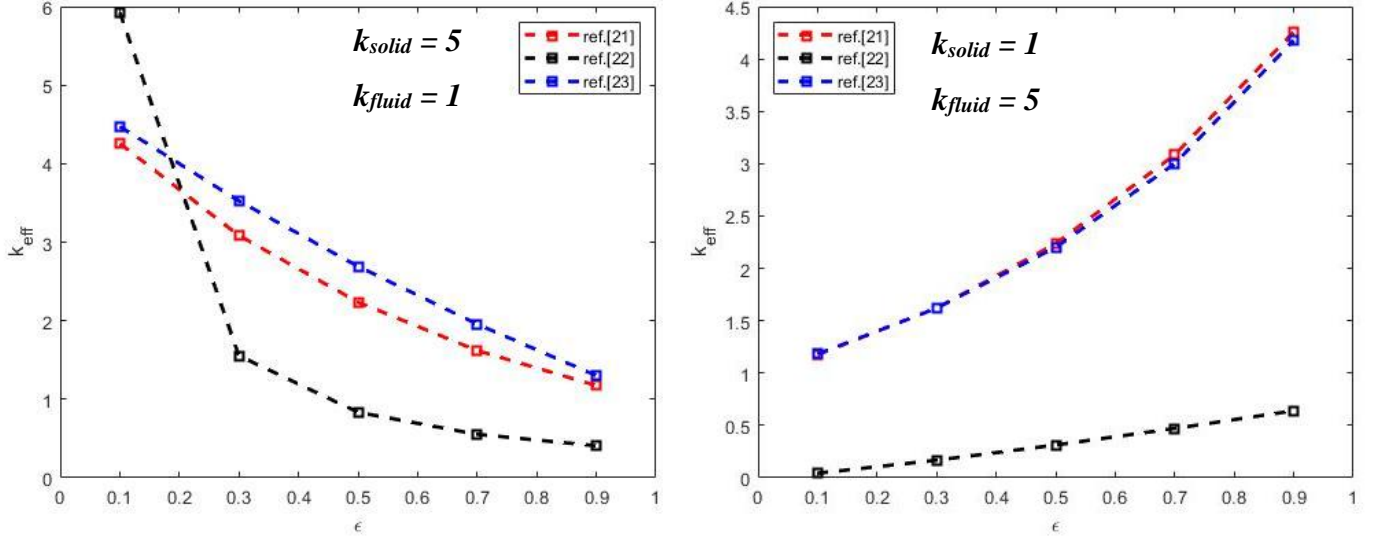


Figure 1.1. Predicted effective thermal conductivity as a function of porosity for (a) $K_{solid} = 5$ W/(m-K) and $K_{fluid} = 1$ W/(m-K) and (b) $K_{solid} = 1$ W/(m-K) and $K_{fluid} = 5$ W/(m-K) based on the models from Ref. 21-23.

1.4 Overview of This Work

Although past work has demonstrated various mechanisms to achieve thermal regulation purposes, continuous tuning of thermal transport across a large range of thermal conductance with an all-solid-state system is still challenging. Many existing thermal regulators have been utilizing mechanisms that associate with liquid, which could be expensive and challenging to implement in applications. Chapter 2 of this work explores compressible foams made of graphene and polydimethylsiloxane (PDMS) polymer as an all-solid-state thermal regulator with continuous tuning. Experimentally, an experimental apparatus is designed to model the heat flow in a thermal system. The temperatures of the designed system are closely monitored to demonstrate the

effectiveness of the graphene/PDMS foam as a thermal regulator. The result shows how the graphene/PDMS foam performs at various levels of thickness, input heat flux, and ambient temperature.

Specifically, this work also explores the thermal transport phenomena of compressed foam-based porous structures. Chapter 3 investigates the change of effective thermal conductivity of polymer foam at compressed and uncompressed states with an infrared microscope. In Chapter 4, a molecular dynamic simulation is performed to investigate trends of thermal conductivity changes along with different directions of a graphene nanofoam. The results provide new insights into the physics of thermal transport in foam-based porous structures.

2. SYSTEM TESTING WITH GRAPHENE/PDMS FLEXIBLE FOAM¹

Graphene is a highly thermally conductive material and could be a good basis for a thermal switch or thermal regulator. However, pure graphene foams are brittle and cannot be directly used as compressible foam structures. Thus, it is necessary to add polymer to improve the flexibility of the graphene foam. In this thesis, a commercially available graphene/PDMS flexible foam (Graphene Supermarket) is chosen to be the thermal switching material. This graphene/PDMS foam is a hybrid material with a CVD grown graphene foam as the core with polydimethylsiloxane (PDMS) appearing to wrap around the graphene filaments (See Figure 2.1). The ratio of composition is 95% CVD grown graphene and 5% polydimethylsiloxane (PDMS). The original foam has a dimension of 76.2×38.1×1.2 mm, a density of 85 mg/cm³ and weighs around 90 g. The pore size of original uncompressed samples is measured to be between 150 to 350 μm as measured from the SEM images in Figure 2.1. The image is taken with a Hitachi S4800 Scanning Electron Microscope.

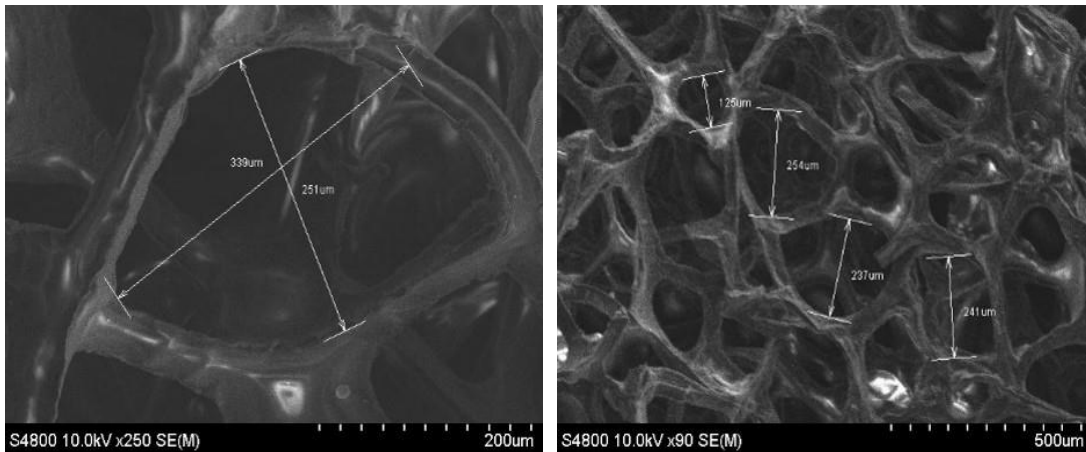


Figure 2.1. SEM images of the porous graphene foam.

It is expected that the graphene/PDMS foam has increasing thermal conductivity and transfers larger amount of heat as its thickness decreases. This prediction is made because of the

¹ Portion of this chapter is shared with a paper prepared to submit to a journal, co-authored by T. Du, L. Delgado, W. Liao, J. Peoples, R. Kantharaj, A. Marconnet and X. Ruan.

increased mass density of the foam. Typically, compression of foams leads to higher density, which will result in higher heat capacity per unit volume to carry the heat, as well as smaller pore size and more contact, or touching, of its supporting structure material. It is also predicted that the sample foam will experience elastic deformation. The thickness of the foam can return to its original state after compression. Thus, adjusting foam thickness is predicted to result in repeatable and controllable thermal resistance, making the graphene/PDMS foam a good candidate for thermal switching material.

To investigate quantitatively how compression will change the effective thermal resistance across the sample foam, a set of experimental apparatus is to be designed.

2.1 Design of the Experimental Apparatus

2.1.1 System Modeling and Analysis

The graphene foam is cut into a square shape with a side of 25.4 mm while the thickness of the graphene foam maintains to be 1.2 mm. As the side is 20 times larger than the thickness, it can be assumed that the heat transfer through the cross-section is a 1D process. Thus, a simple 1D heat transfer model can be created using Fourier's Law.

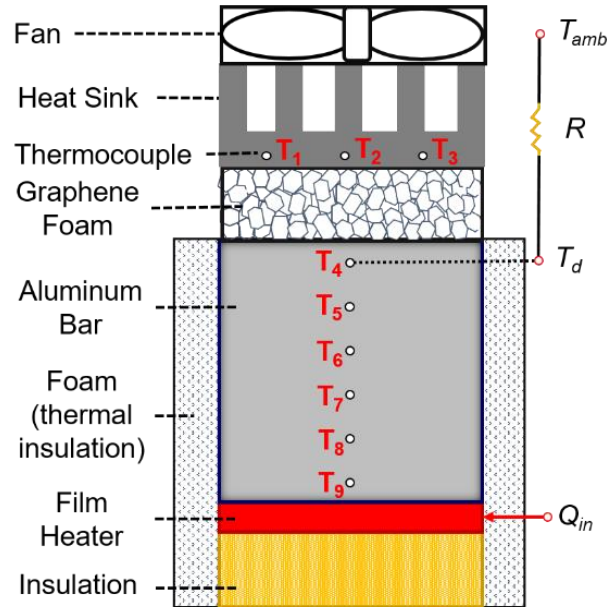


Figure 2.2. Schematic Diagram and thermal circuit of the simplified system.

The design concept shown in Figure 2.2 includes a fanned heat sink, the graphene foam, an aluminum bar, a flexible polyimide heat, and a plastic bar as an insulator. The graphene foam is placed between the fanned heat sink and the aluminum bar. Heat current flows upward from the flexible heater, through the aluminum heat spreader, the graphene foam, the fanned heat sink, and finally to be dissipated into the ambient air. The plastic insulator is placed underneath the heat to direct most of the heat flux to flow upward into the aluminum bar.

The fanned heat sink enhances heat dissipation. The aluminum bar serves as a heat spreader that ensures a uniform heat flux flowing into the graphene foam. Nine holes (three on the heat sink and six on the aluminum bar) are punched for temperature measurements. By analyzing the temperature difference across the foam, the tunability of the graphene foam thermal switch can be determined. Another purpose of the experiment is to find out the range of the heat sink temperature at different given input heat flux.

2.1.2 Experimental Setup Design Concepts and Expectations

The experiment aims to demonstrate this adjustable heat transfer characteristic. The design contains several essential concepts. 1) The adjustability of heat flux that flows through the foam. Necessary measurements are to be taken to quantitatively analyze the heat transfer process. 2) The thickness of the foam needs to be adjustable and accurately measured. Manual control is sufficient for this purpose. 3) The experimental setup needs to be easy to make, easy to use, and reliable in terms of obtaining accurate measurements.

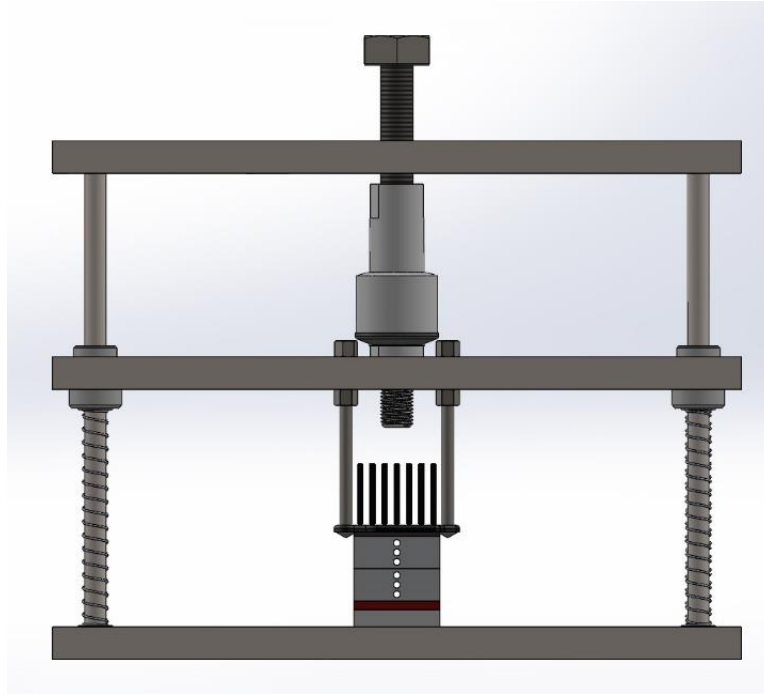


Figure 2.3. CAD model of the system testing design concept.

Besides the key components shown in Figure 2.2, A CAD model using SOLIDWORKS® of the initial design concept is shown in Figure 2.3. The design consists other important components including three aluminum plates (top, middle, and bottom), four supporting rods, an inline ball joint linkage, and two smaller rods to attach the heat sink to the plate.

The setup can be divided into two sections, the fixed section, and the moving section. The fixed section consists the bottom and top plates with the supporting rods. The moving section includes the aluminum bar, the heater, and the insulator are stacked at the center of the bottom plate. The moving section includes the middle plate with the fanned heat sink attached, the inline ball joint linkage, and the threaded rod. Four linear sleeve bearings serve to allow smoother sliding between the middle plate and the supporting rods.

The thin and soft nature of the graphene foam prevents any type of attachment that may cause unintended deformation. Thus, the adjustability of foam thickness is achieved by a rotatable threaded rod that controls vertical movements of the middle plates through the inline ball joint linkage. The ball joint linkage transfers rotational motion to linear motion, which minimizes non-vertical movements of the middle plate. The addition of springs around the rods serves to support the linear bearings and reduce the difference in the bearings' vertical displacement.

2.1.3 Actual Experiment Setup

The actual experimental setup is machined and built by the precision machine shop from the Department of Chemistry of Purdue University.

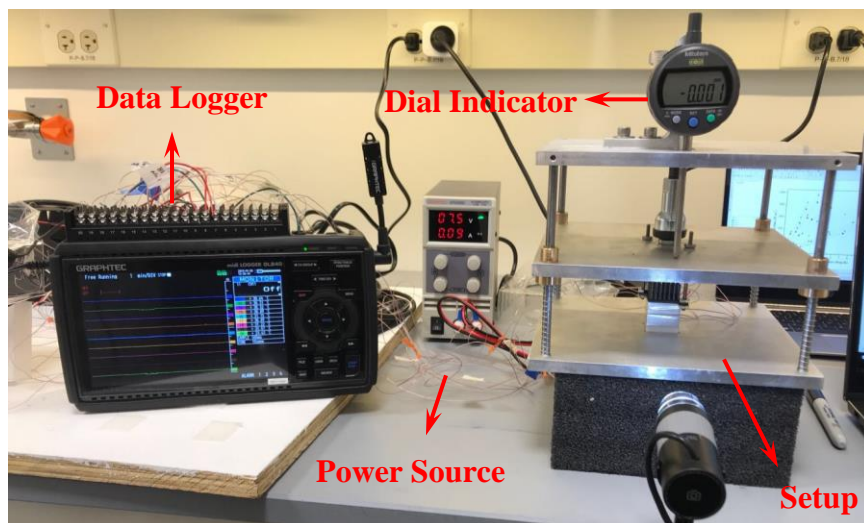


Figure 2.4. Actual experimental setup with power supply and data logger.

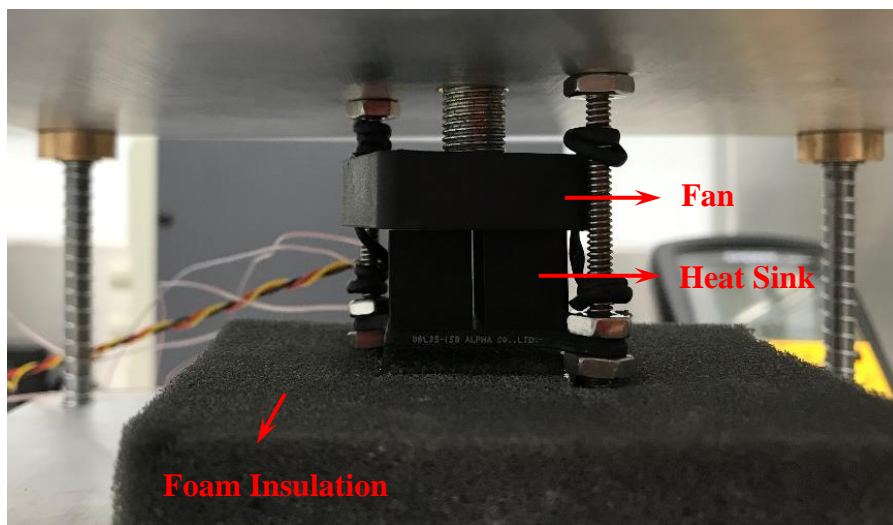


Figure 2.5. A closer look at the core section of the experimental setup, as only the fanned heat sink and the graphene foam are exposed to ambient air. The aluminum bar and the input heat source are insulated by packing foam.

Figure 2.4 and Figure 2.5 show the entirety of the experimental setup with supporting devices and tools. The material chosen for the plates is aluminum for its lightweight and machinability. The supporting rods and the threaded rod of the inline ball joint linkage are made of stainless steel for better durability.

The Mitutoyo electronic dial indicator (ID-C 543-Standard Type) is mounted on top of the top plate. The contact needle extends down on the middle plate to measure relative vertical displacement. It is assumed that this displacement is equivalent to the change in the graphene foam thickness. The power supply (DC, 0-30V, 0-5A, Eventek) provides the heat input into the system. A data logger (Graphtech Midi Data Logger GL840) and a total of ten T-type thermocouples are used to measure and record temperatures throughout the system. Nine of the thermocouples are inserted into the small holes as shown in Figure 2.2, and one hanging in the air is to measure the reference ambient temperature. The holes are filled with thermal paste (ARCTIC MX-4) to reduce the contact resistance between the aluminum surface and the thermocouple wires. The heat sink used in this experiment (Alpha Novatech UBL25) is chosen with the consideration of having the lowest equivalent thermal resistance under active cooling conditions. The aluminum bar is well exposed in the air, causing a significant amount of convective heat loss. Thus, a large piece of packing foam is placed covering it. The packing foam is tested to be a good insulator, which allows the analysis to be one-dimensional.

2.2 Testing and Results

The experiment has three variables: foam thickness, input heat flux, and ambient temperature. To quantitatively understand how each of these variables affects the heat transfer performance, two sets of experiments are carried out. The first set will keep the ambient at room temperature, while the second set will be conducted in an environmental chamber with fixed input heat flux. All other conditions of the experiments are to be remained the same.

The uncompressed foam thickness is 1.2mm. The fully compressed foam thickness is measured to be 0.086mm.

2.2.1 Testing under Ambient Temperature

The experiment is carried out in a small room, which minimizes the random factor of airflow as well as changes in the ambient temperature. Throughout the entire experiment, the ambient temperature stays between 20 and 22 degrees Celsius. From the aspect of a practical experiment, this temperature variation is low enough to be accepted as a constant ambient temperature condition.

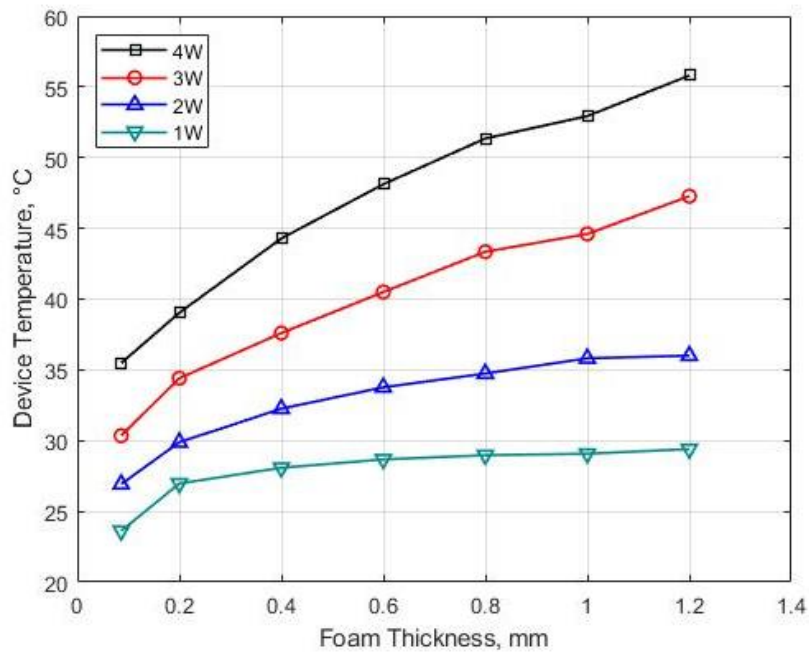


Figure 2.6. The device temperature with respect to foam thickness at various input heat flux under room temperature.

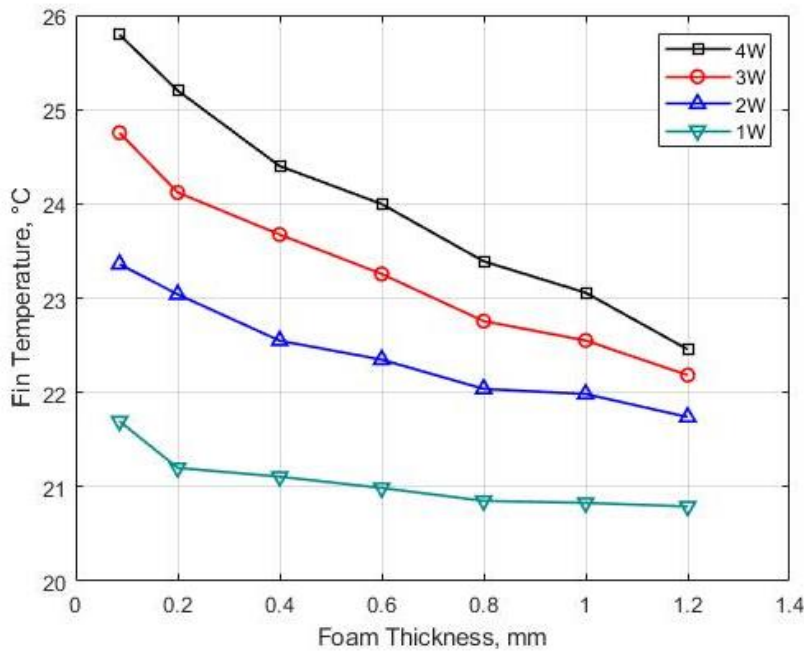


Figure 2.7. The fin temperature with respect to foam thickness at various input heat flux under room temperature.

The temperature of the aluminum (referred as the device temperature) and the temperature of the fin (referred as the fin temperature) are collected. The fin temperature is obtained by taking the mean value of the three temperature measurements on the fin, T_1 , T_2 , and T_3 . The device temperature is obtained by taking the mean value of the measurements from the three upper holes, T_4 , T_5 , and T_6 . The six measurements on the aluminum bar are observed to be very similar, to an extent that the differences are well below the combined uncertainty of the thermocouple and the data logger.

Figure 2.6 and Figure 2.7 show the trends of how temperatures of the device and the fin react to the change of foam thickness. At each level of input heat flux and when the foam is more compressed, the device temperature decreases, and the fin temperature increases. For the device temperature, it can be observed that the level of temperature drop is more significant when the input heat flux is higher. The device experiences a 5-degree Celsius difference between the two extreme heat flux conditions, and the temperature difference becomes over 10 degrees Celsius when the heat flux is increased to $6,054 \text{ W/m}^2$.

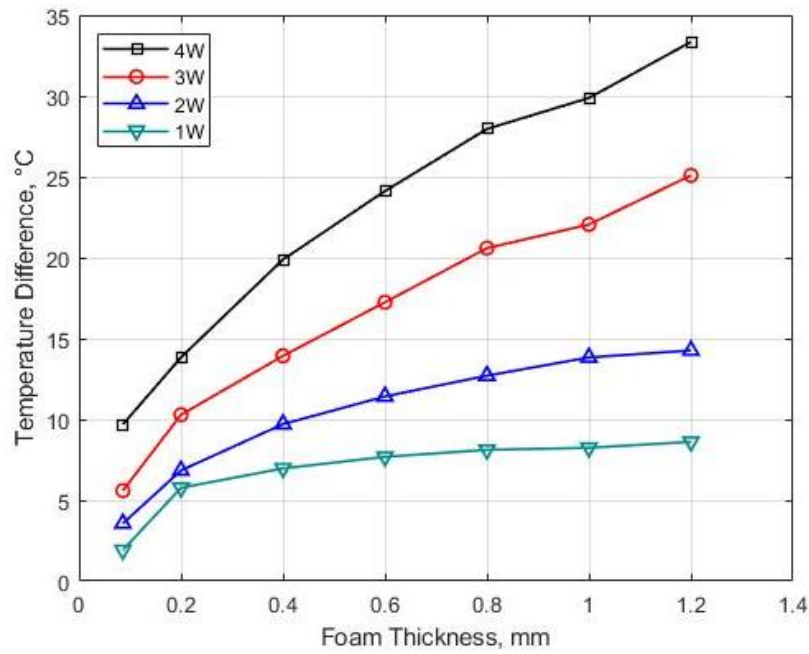


Figure 2.8. The temperature difference across the graphene foam with respect to foam thickness under room temperature.

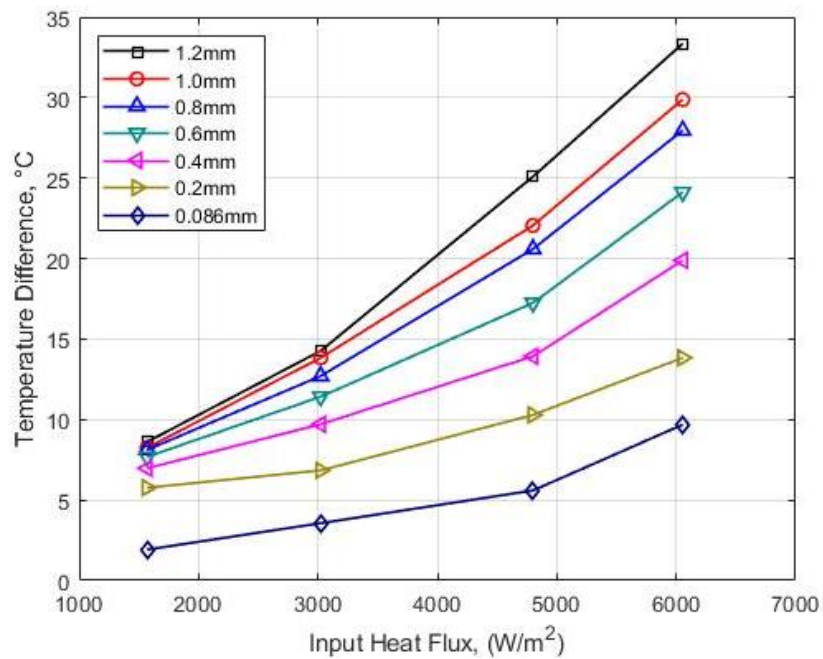


Figure 2.9. The temperature difference across the graphene foam with respect to input heat flux under room temperature.

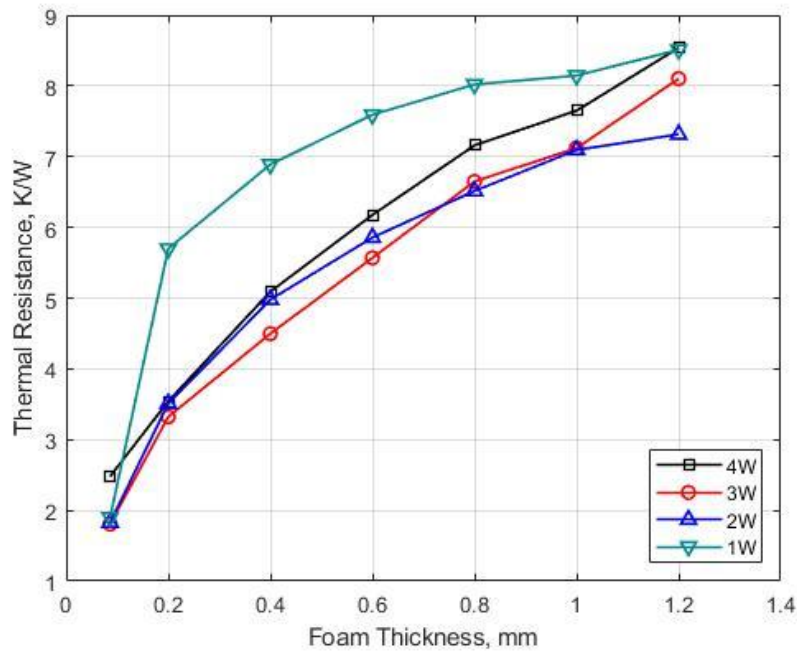


Figure 2.10. Calculated thermal resistance as functions of foam thickness at each input heat flux level under room temperature.

However, a more important quantity of this experiment is the temperature difference across the graphene foam, as shown in Figure 2.8 and Figure 2.9, which leads to the thermal resistance of the foam, as shown in Figure 2.10. Comparing to the uncompressed state, there are significant reductions in Temperature difference when the foam becomes compressed. For thermal resistance calculation, it can be observed that the result with low heat flux level returns higher thermal resistance value. However, the rest three curves show constant thermal resistance values at each thickness level, and all data shows the thermal resistance increases as foam thickness increases. The uncompressed state has a thermal resistance of $\sim 8 \text{ K/W}$, while the compressed state has $\sim 2 \text{ K/W}$. This results in a switching ratio of ~ 4 . This shows that using graphene foam has great potential in temperature regulation applications.

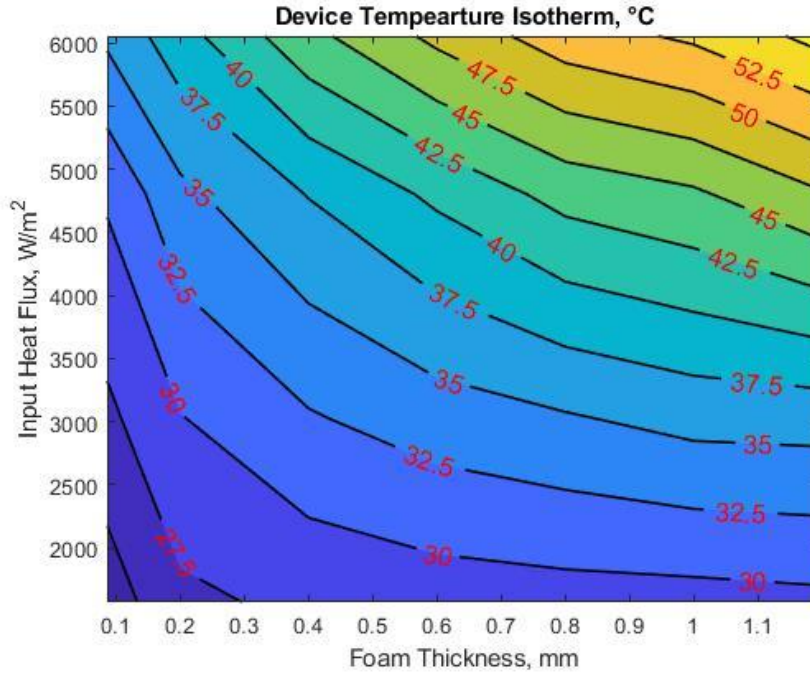


Figure 2.11. A contour plot showing how foam thickness and input heat flux affect the resultant device temperature under room temperature.

As for thermal switching application, a tunability map showing isotherms can be derived from Figure 2.6, as shown in Figure 2.11. A desired temperature can be achieved by using the correct combination of heat flux and foam thickness. This tunability map also suggests the effectiveness of the foam thickness as a continuous thermal switch. For instance, if the system requires a heat dissipation level of $4,500 \text{ W/m}^2$, the device temperature can be maintained between 30 and 45 degrees by changing the foam thickness. The temperature difference between the device and the ambient can be controlled between 10 and 25 degrees, which achieves a tuning window of 15 degrees Celsius.

2.2.2 Testing in Environmental Chamber

As mentioned, one great usage of a thermal switch is to regulate device temperature under different ambient environments. Many applications desire narrow ranges of optimal operating temperatures. This set of experiments aims to demonstrate the effectiveness of the graphene foam thermal switch in maintaining this range of optimal temperature.

To see how the device temperature reacts to change in ambient, the apparatus is placed in an environmental chamber. This chamber can maintain temperature from 0-30°C. To ensure that the ambient temperature is held constant as possible, the chamber is closed throughout each set of tests. For each trial, the thickness of the foam and the input heat flux is held constant while the chamber temperature is changed once the system reaches steady-state. The device temperature is recorded.

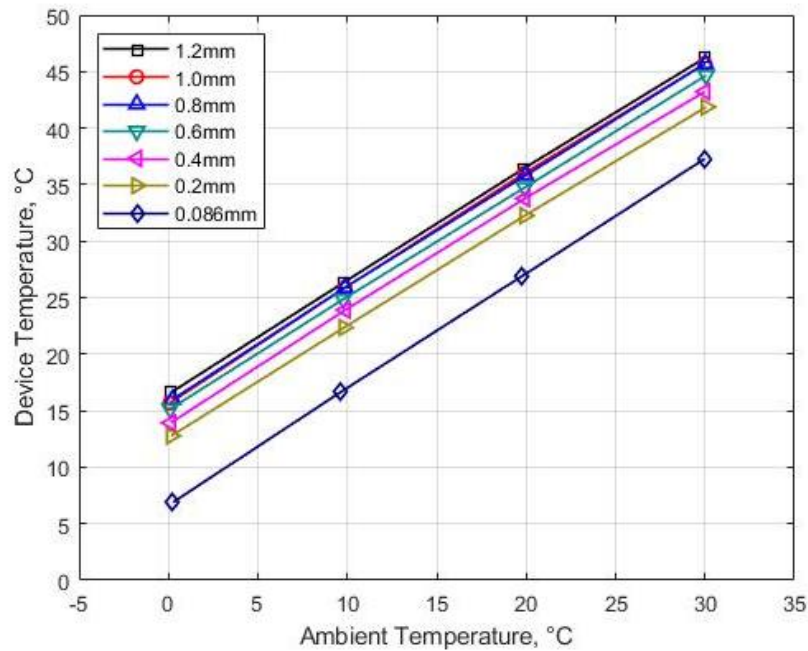


Figure 2.12. The device temperature with respect to the ambient temperature at each thickness level in the environmental chamber.

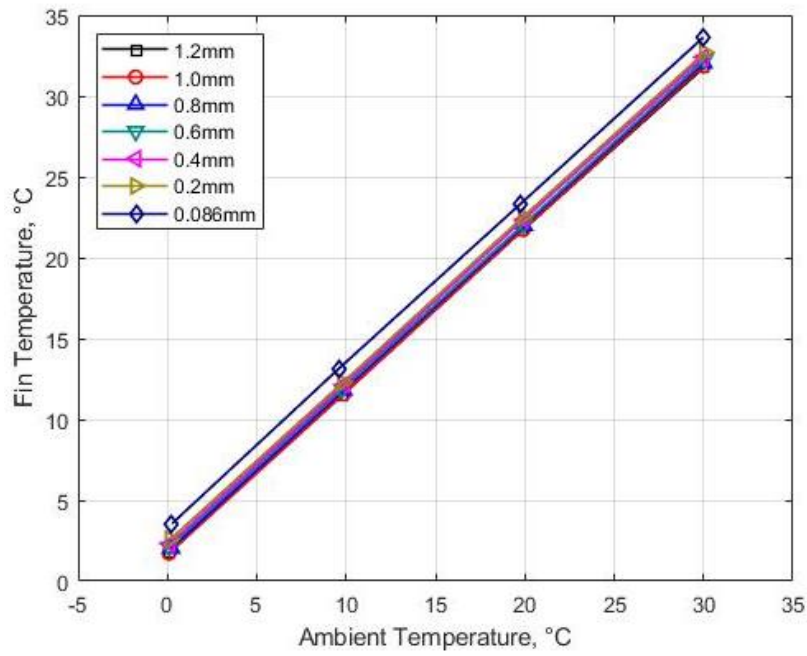


Figure 2.13. The fin temperature with respect ambient temperature at each thickness level in the environmental chamber.

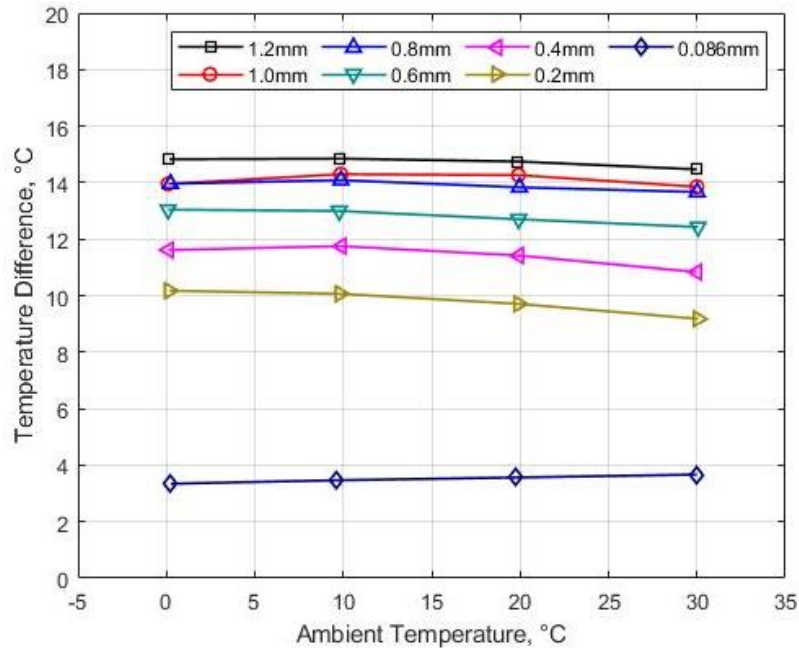


Figure 2.14. The temperature difference across the graphene foam with respect to ambient temperature in the environmental chamber.

The chamber experiment shows a good level of consistency in effective thermal resistance calculations. Figure 2.12 shows the device temperature as a function of the ambient temperature. It can be observed that this relationship is linear at all thickness levels and they appear to have a very similar temperature gradient of 1. Figure 2.13 shows the fin temperature as a function of the ambient temperature. At different thicknesses, the fin temperature is independent with foam thickness. This confirms that the heat flux is maintained as a constant because the fanned heat sink has a constant thermal resistance. Furthermore, with a temperature gradient approximately equals to 1, the heat sink temperature is about 2.5 degrees higher than ambient at all times. As temperatures on each side of the graphene foam exhibit similar behavior, the differences between them are also independent of ambient temperature, as shown in Figure 2.14.

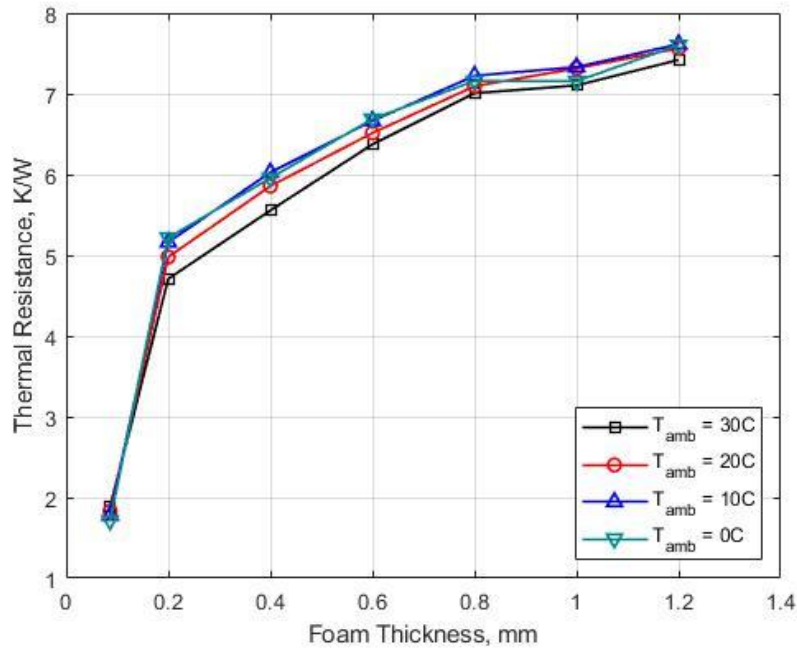


Figure 2.15. Thermal resistance of the graphene foam as functions of foam thickness at each input heat flux level.

The thermal resistance of the graphene foam increases as its thickness increases, but is independent with ambient temperature, as shown in Figure 2.15. This shows that the graphene foam is capable of performing temperature regulation tasks under both cold and hot environments.

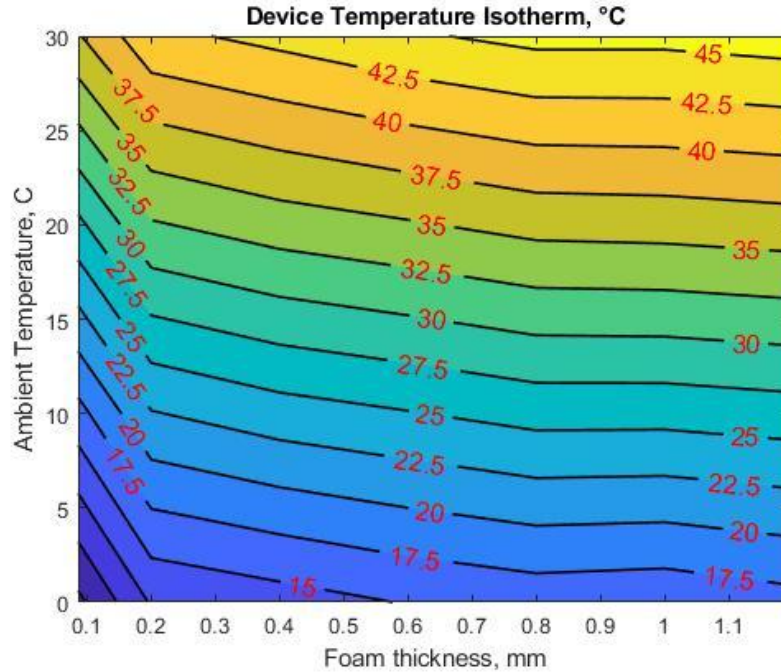


Figure 2.16. A contour plot showing how foam thickness and input heat flux affect the resultant device temperature in the chamber.

Figure 2.16 shows the device temperature map with isotherms similar to Figure 2.11. A desired device temperature can be achieved with the correct combination of ambient temperature and foam thickness. For instance, if the ambient air is at 25°C, the device is to be maintained anywhere between 32.5 and ~41°C by changing foam thickness. If the ambient is at 5°C, the device is able to stay between 12.5 and ~22°C. This way in a cold environment, the device can be maintained at a much higher temperature to avoid freezing and therefore maintain normal operations. While in a hot environment, the high thermal resistance of the switch can be tuned to avoid the risk of being overheated.

2.3 Reliability and Cycling Test

Elastic deformation is the basic mechanism of using a foam-based structure to achieve temperature regulation. The foam needs to be able to restore to its original state shortly after the pressure is released. As the sample is often compressed to the maximum condition, it is uncertain if the foam still practices elastic deformation.

A visual inspection and thickness measurement of the foam shows no difference prior and after the foam is compressed. However, to ensure the material can keep this performance for an extended period of time, a reliability test is carried out to test the durability of the graphene foam. The ambient temperature is set at 20°C. Similarly, the temperatures are measured when the graphene foam is uncompressed and fully compressed. This procedure is repeated 10 times within a span of two days.

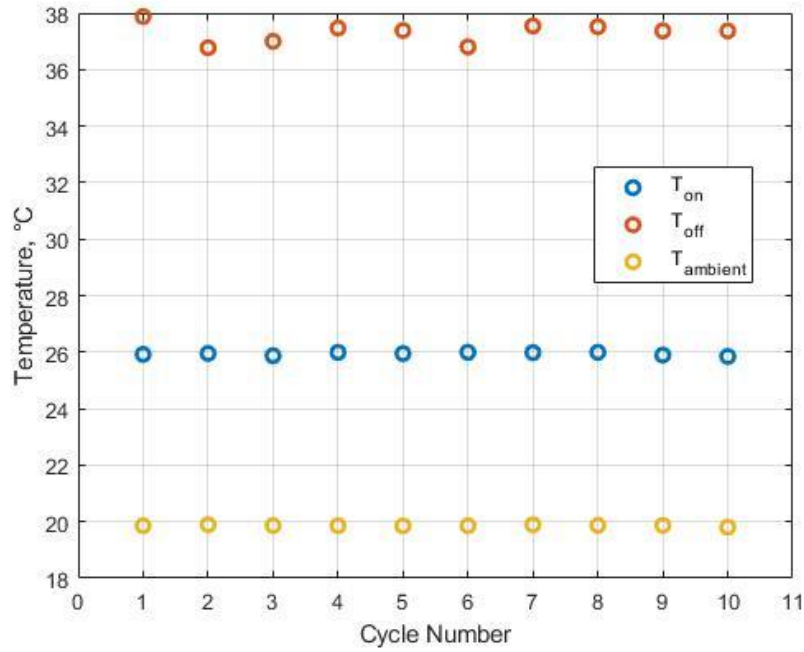


Figure 2.17. Temperature measurements for the reliability test of the graphene foam.

In Figure 2.17, the ambient temperature is kept constant at 20°C. When the foam is compressed, the device temperatures are measured to be between 36.8°C and 37.9°C. When the foam is uncompressed, the device temperatures are measured to be between 25.9°C and 26.0°C, which has negligible uncertainty. All temperature measurements do not show trends to either increase or decrease. This reliability test demonstrates that using graphene foam as a temperature regulation application is reliable and can maintain its performance for an extended period of time.

2.4 Discussions and Conclusion

In general, the experiments have demonstrated the thermal resistance tuning ability of the compressible graphene-polymer foam. The switching ratio can be as high as ~ 4 while having a continuous tuning capability.

This device-focused experiment emphasizes the graphene-polymer foam as a thermal resistor, as it is the more effective way to demonstrate how temperature is regulated. In the room temperature test, an interesting pattern of the fin temperature is that the values are very similar when the thickness is small, and the temperature drops as the thickness increases. Theoretically, the heat sink has a constant equivalent thermal resistance. This means the temperature difference between the fin and ambient air should be constant if the heat flux is constant. As the fin shows a larger temperature difference when the foam becomes uncompressed, it suggests that the heat flux flowing through the foam isn't constant. This can be explained by analyzing the overall heat flow of the system. Since the flexible polyimide heater is a double-side heater, heat flows toward both the upper side (the aluminum bar) and the bottom side (the insulator). When the foam is uncompressed, the foam is essentially a thermal insulator. Thus, there will be a considerable amount of heat flowing to the insulator and dissipating elsewhere. The equivalent thermal resistance of the upper side (the aluminum bar, the foam, and the fin) and the thermal resistance of the bottom insulator decides the distribution of this heat flow. As the foam is compressed, the thermal resistance of the upper side will be reduced, causing more heat flux to flow through the foam and resulting in an increase in the fin temperature.

Another interesting observation that can be made from Figure 2.15 and Figure 2.16 is that compressing the foam toward maximum compression results in a much more dramatic change in the results than that of other levels. This is due to the fact that the branches of the foam are pushed together and results in better contact among each other, hence reducing thermal resistance. It can also be observed that the temperature difference is not really changed when the foam close to the uncompressed state. This suggests that even though the density of the foam is reduced, it does not necessarily lead to better contact between the branches. This means that the thermal switching capability is more effective when the foam is more compressed, and vice versa.

3. VARIABLE THERMAL CONDUCTIVITY AND CONDUCTANCE OF COMPRESSIBLE POLYMER FOAM

The graphene/PDMS flexible foam has demonstrated a good capability in temperature regulation applications, but there is a need to push the low and high conductance states. The graphene foam achieved a wide range of effective thermal resistance with a switching ratio of about ~4. As that foam was only 1.2mm in thickness, a thicker foam may be able to achieve even higher switching ratio because the uncompressed sample could have a larger thermal resistance. Furthermore, the effective thermal resistance measured in the previous experiment is only applicable to the specific setup because of the parasitic heat losses. It is important to directly measure the effective thermal conductivity of foams, which can be widely applied to other setup and applications and provides insight into the fundamental transport mechanisms.

For this portion of the work, ordinary packing foam is selected as the switching material. This is due to the fact that packing foam is highly compressible and can be cut to achieve the form factor desired for this experiment.

The primary purpose of this experiment is to measure the effective thermal conductivity of foam-based structure as a function of the compression level. The solid material used to construct the foam structure has its own intrinsic thermal conductivity. However, foams are porous with a large portion being air, which lowers the effective heat transfer capability of the material. Thus, the intrinsic thermal conductivity of the material is not directly useful in application. Thus, an effective thermal conductivity, which considers both the air and the solid material, is more useful to predict the heat transfer behavior of the structure. The foam sample in this chapter also needs to be thicker when uncompressed as the secondary purpose is to quantitatively investigate if a thicker foam can give better results in terms of switching.

3.1 Experimental Setup and Method

To measure the intrinsic thermal conductivity, a steady-state miniaturized reference bar method is used [24]. To achieve this, it is important to determine the actual heat flux that is flowing through the foam sample, which the experiments in Chapter 2 do not directly measure. In this experiment, an infrared camera (QFI MWIR-1024) is used to obtain precise, two-dimensional

steady-state temperature maps, which will allow reliable determination of actual heat flux (through measurements of the temperature gradient in a known material) and the temperature gradient in the sample region. Using Fourier's Law, the unknown thermal conductivity of the sample region can then be determined.

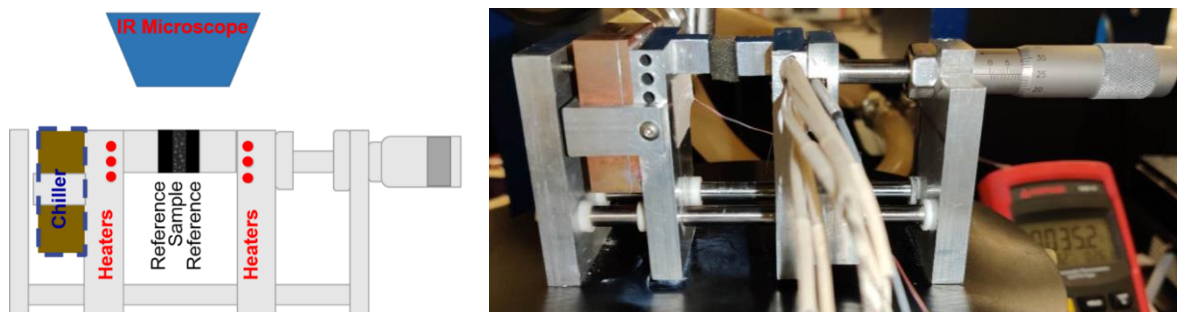


Figure 3.1. (Left) Schematic and (Right) photograph of the experimental setup for the miniaturized reference bar method with temperature measurements obtained with an infrared (IR) microscope.

Figure 3.1 shows the experimental apparatus for the IR microscope-based experiment. The sample is sandwiched between two pieces of reference material, which has a known thermal conductivity of 0.3 W/(m-K) . The cross-section of both the sample and the reference layers is 10 mm by 10 mm. The uncompressed thickness of the foam is $\sim 9 \text{ mm}$ and the thickness of the reference material is $\sim 6 \text{ mm}$. The bars that transfer heat to and from the sample, as well as compress the sample, are aluminum. A chiller, connected to a water circulation system, keeps the left side at a constant temperature that is slightly above room temperature and is thus referred to as the “cold side”. The right side, or the “hot side”, is heated with cartridge heaters with controlled power levels. The sandwich structure can be compressed via the micrometer on the right. Thermocouples on both the hot and cold aluminum bars are used during the experiment for reference and calibration purposes. The spatially-varying emissivity of the sample and reference layers are needed to ensure the temperatures during measurement are accurate. The emissivity is calibrated when the sample stack is at a known and uniform reference temperature (measured the thermocouple readings).

Once the emissivity is calibrated, temperature data is acquired with the IR microscope, and this thermal data is used to calculate the thermal conductivity of the sample. Specifically, for each compression level, four temperature maps associated with four levels of input heat flux will be

collected to derive the effective thermal conductivity. Using Fourier's law, the heat flux will be determined from the two reference materials.

Note that since the foam is held from the sides by the aluminum bars, there must be enough shear friction force to avoid the sample falling due to gravity. Thus, the "uncompressed" state discussed in this section is actually slightly compressed to ~6.3 mm (from the original ~9 mm). For the fully compressed state, the thickness is reduced to 0.55 mm. This allows a thickness ratio over a factor of 10.

3.2 Assumptions and Determination of Analysis Methods

The data analysis process is similar to that of the graphene foam system experiment in Chapter 2. However, the focus of the experiment has shifted from the system-level performance of the device to the property of the compressible material.

A major challenge after the increase in foam thickness with the current setup is the impact of convective heat loss through the sides of (and within) the foam. In the compressed state test, the sides are relatively small in area compared to the cross-sectional area. Comparing the convective losses at the edges to the conduction through the sample with expected property values, it is likely in the compressed state convection losses will be negligible. However, there will be significant heat loss in the uncompressed state because the surface area exposed to convection is much larger than that of the compressed state. If this assumption holds, then different methods will be required to analyze the two states.

Under both conditions (fully compressed and uncompressed), the experiment procedure is identical. The foam is subjected to temperature gradients with the heater power source set to be 11V, 15V, 19V, and 23V. Temperature maps at each power level are taken to reduce random error from a single temperature map. Each temperature map is divided into three regions: two references and the sample. The temperature gradient and the size of each region are calculated to determine thermal conductivity.

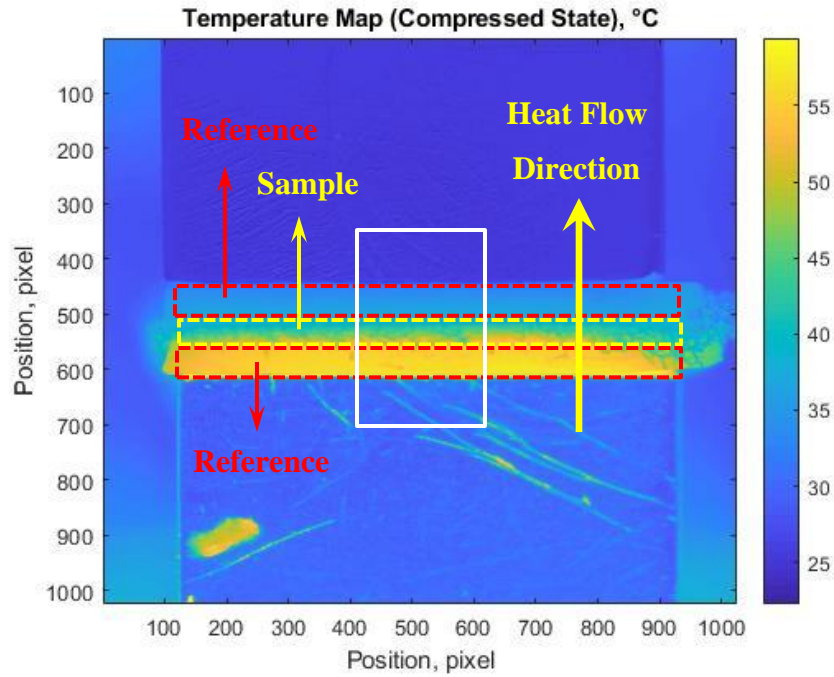


Figure 3.2. Example temperature map showing the temperature distribution of the sandwich structure at the *compressed* state, with the white box indicating the selected region for analysis. Each pixel is approximately $12\ \mu\text{m}$.

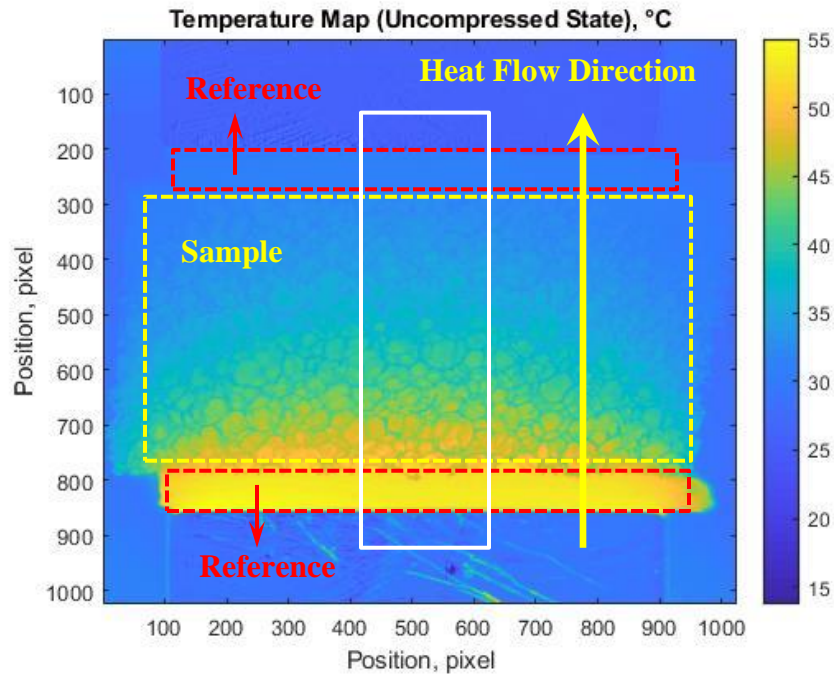


Figure 3.3. Example temperature map showing the temperature distribution of the sandwich structure at the *uncompressed* state, with the white box indicating the selected region for analysis. Each pixel is approximately $12\ \mu\text{m}$.

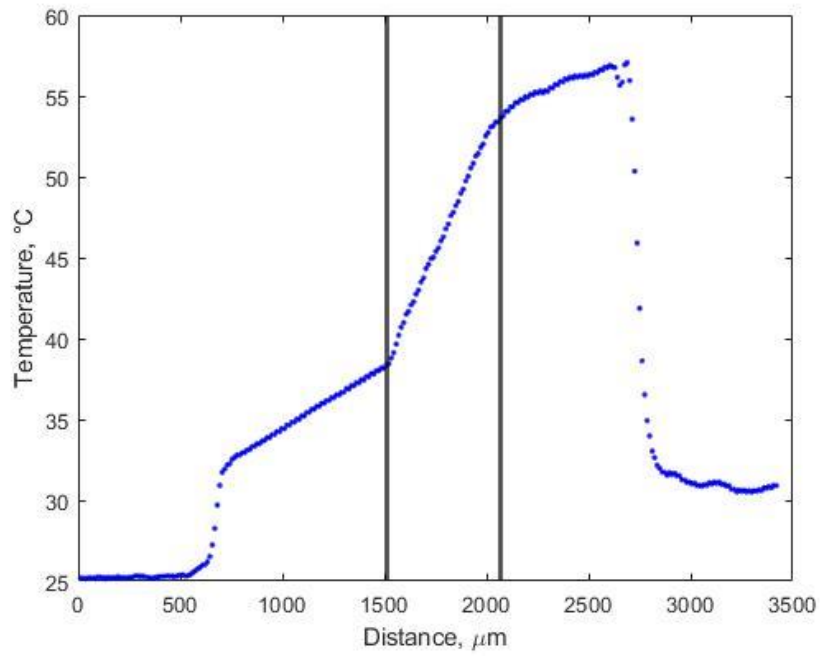


Figure 3.4. Example temperature profile along the heat flow direction for the *compressed* state.

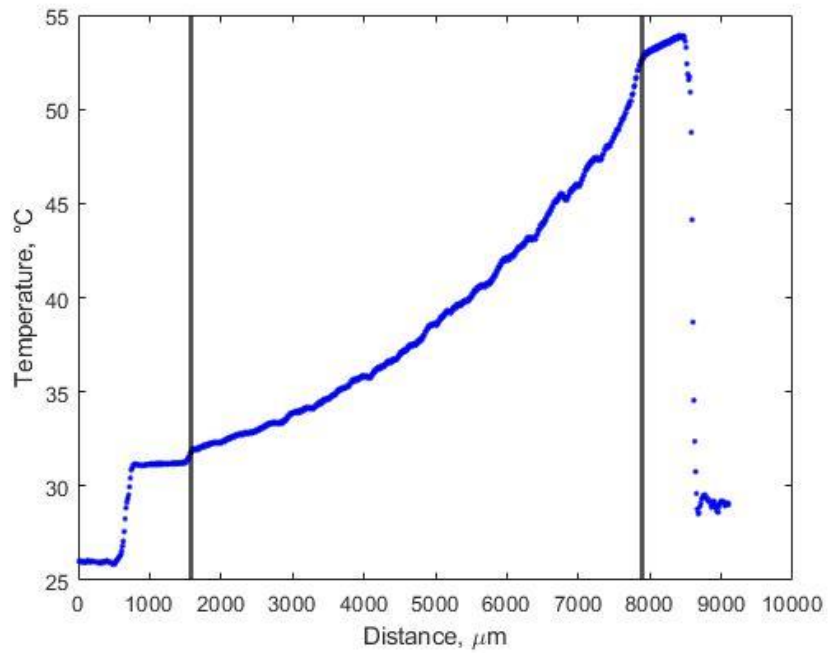


Figure 3.5. Example temperature profile along the heat flow direction for the *uncompressed* state.

The temperature map shown in Figure 3.2 (compressed) and Figure 3.3 (uncompressed) are at the highest input heat flux, in which the highest temperature of the system reaches 58°C. For analysis purposes, this image is rotated so that the heat flows along the vertical along the y-axis, with the top being the cold side and the bottom being the hot side. The red boxes shown on the figures are the selected region for data analysis. A small region is selected for analysis to evaluate if the convective heat loss can be neglected.

The temperature profiles shown in Figure 3.4 and Figure 3.5 are obtained by taking the average of all data points within each horizontal row within the red boxes. When analyzing the 1-D profile, the edges of the sample (indicated with the black boundary lines in Figure 3.4 and Figure 3.5) are manually selected based on the temperature profile. After obtaining the 1-D temperature profiles, the boundaries are clear to distinguish based on the change in slope and the boundary resistance is small (*i.e.*, minimal vertical jump at the sample-reference interfaces).

More importantly, comparing the temperature profiles show the significance of the convective heat loss. For the compressed state, as shown in Figure 3.2 and Figure 3.4, the temperature profile in the sample region is linear, which suggests that convective heat loss has a negligible effect on the system. In contrast, the profile is not linear for the uncompressed state, as shown in Figure 3.3 and Figure 3.5, which suggests heat loss by convection takes a significant role in this process. Therefore, the compressed state test can be analyzed by Fourier's Law assuming a one-dimensional model. However, convective heat transfer must be considered in the uncompressed state. Thus, it requires different methods to determine the effective thermal conductivity of the foam and the equivalent convective heat transfer model.

3.3 Experiment Results and Analysis

From the 1-D temperature profiles described in the previous section, a standard analysis neglecting convection is sufficient to calculate effective thermal conductivity only for the compressed state. Convective heat loss must be included in the uncompressed state, which means both the effective thermal conductivity and the effective convective heat transfer coefficient will be calculated. Specifically, for the compressed state analysis, a one-dimensional conductive heat transfer model using Fourier's Law will be applied. For the uncompressed state, three methods are evaluated with increasing levels of fidelity: using a near-interface 1-D conduction approximation,

applying the one-dimensional fin equations, and simulating the 3-D geometry in COMSOL Multiphysics® software.

3.3.1 Compressed State

The temperature gradient in each region is calculated by applying linear fitting to the three regions (hot side reference, sample, and cold side reference). The heat flux through the sample can be calculated by averaging the heat flux flowing through the hot and cold sides:

$$q''_{ref} = \frac{W_{ref}}{A_c} \int_0^H k_{ref} \frac{dT}{dx} dy = k_{ref} \overline{\left(\frac{dT}{dx}\right)}, \text{ and} \quad (3.1)$$

$$q''_{ave} = \frac{1}{2} \sum k_{ref} \left(\frac{dT_{ref}}{dx}\right), \quad (3.2)$$

where, W_{ref} is the depth into the page, H is the size of the analyzed region (1.0 mm), and A_c is the cross-sectional area of the selected data analysis region.

Table 3.1. Power Source Voltage, Temperature Gradients, and Heat Flux for the *Compressed* Packing Foam Experiment

Temperature Map No.	Power Source Voltage (V)	Temperature Gradient (K/mm)			Heat Flux (kW/m ²)
		Cold Ref.	Sample	Hot Ref.	
1	11.0	1.28	6.58	0.85	0.32
2	15.0	3.17	15.06	2.14	0.80
3	19.0	5.69	24.55	3.57	1.39
4	23.0	7.39	31.95	4.86	1.84

The overall effective thermal conductivity is calculated considering Fourier's Law for heat conduction through the sample:

$$q''_{ave} = k_{eff} \left(\frac{dT_{sample}}{dx} \right) \quad (3.3)$$

While analyzing a single heater power can yield data for effective thermal conductivity, here, 4 power levels are considered as shown in Figure 3.6. Fitting the heat flux as a function of temperature gradient in the sample yields an effective thermal conductivity of the compressed packing foam at a thickness of 0.55 mm is $\sim 0.057 \text{ W}/(\text{m}\cdot\text{K})$. Considering the uncertainties in input heat flux obtained from the two references, the result of compressed foam thermal conductivity is $0.057 \pm 0.012 \text{ W}/(\text{m}\cdot\text{K})$. All trials have shown consistent results.

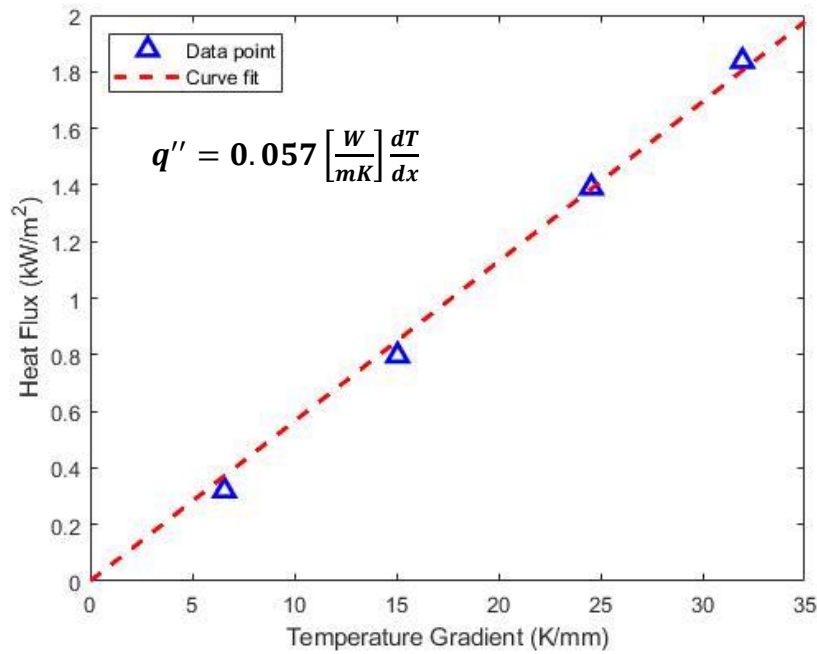


Figure 3.6. Heat flux through the sample in the *compressed* state as a function of the sample temperature gradient. The red dashed line shows the best fit (with fixed y-intercept), the slope of which is the effective thermal conductivity of compressed packing foam.

3.3.2 Uncompressed State: Near-Interface Approximation

One simple method to find an approximated effective thermal conductivity is to focus only on the small region that is close to the hot side boundary where the temperature gradient is

approximately linear. From Figure 3.5, the temperature profile in the entire sample region is clearly nonlinear due to the convective heat loss. However, we can approximate the temperature profile as linear in a small region to the left of the hot-side sample-reference interface.

To understand how “linear” the profile is in the near-interface region, the local temperature gradient is calculated to help observe how the temperature gradient changes at each local position. This gradient is obtained by applying linear fitting to a small number of data points starting from point 1, which is the first point to the left of the hot sample-reference boundary, and then gradually moving away from the boundary line pixel-by-pixel.

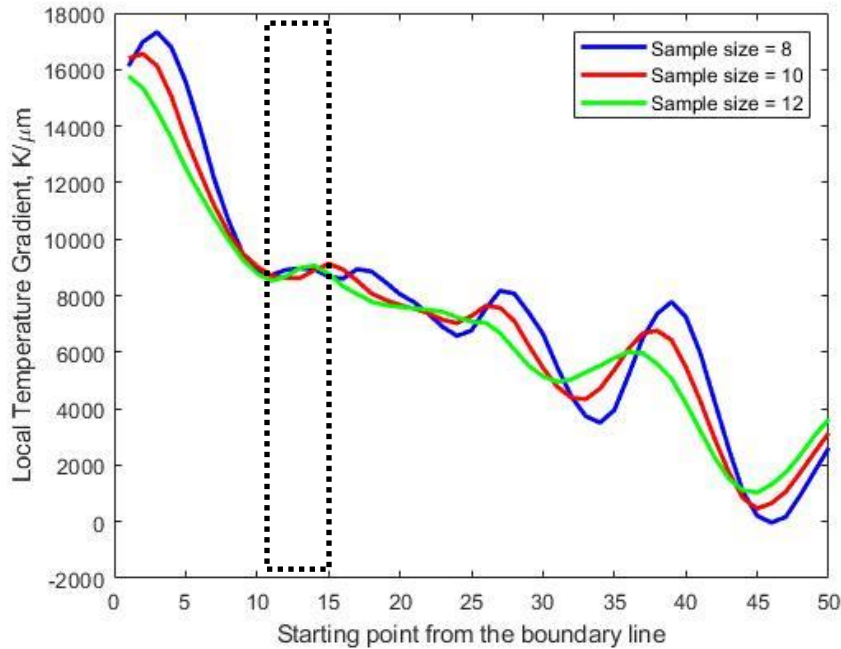


Figure 3.7. Moving average of local temperature gradient for near-interface analysis with different sample windows for the derivatives.

A small region of stable local temperature gradient can be seen with sample sizes of 8, 10, and 12 in Figure 3.7. This stable region happens in the region starting from data point No. 11. This suggests that the local temperature profile is linear in the small region from data point No. 11 to, approximately, data point No. 25. Thus, the local temperature gradient in this region is used to calculate the effective thermal conductivity using the same method as for the compressed sample in section 0. For this sample, the stable temperature gradient is estimated to be ~ 8.7 K/mm within

the sample. After obtaining the temperature gradient, the same method used in section 3.3.1 can be applied. The result using near-interface approximation yields an effective thermal conductivity of $\sim 0.057 \text{ W/(m-K)}$. This value is very similar to the one obtained from the compressed foam experiment. This result provides an interesting insight into the conduction phenomena: the effective thermal conductivity may not be directly related to the level of compression for these foams.

Table 3.2. Temperature Gradients and Heat Flux for the *Uncompressed* Packing Foam Analysis by Near-Interface Approximation.

Temperature Map No.	Hot Ref. Temperature Gradient (K/mm)	Near-Interface Temperature Gradient (K/mm)	Hot Side Heat Flux (W/m ²)
1	0.447	3.84	134.2
2	0.847	6.27	254.1
3	1.63	8.69	488.1
4	2.50	11.72	750.8

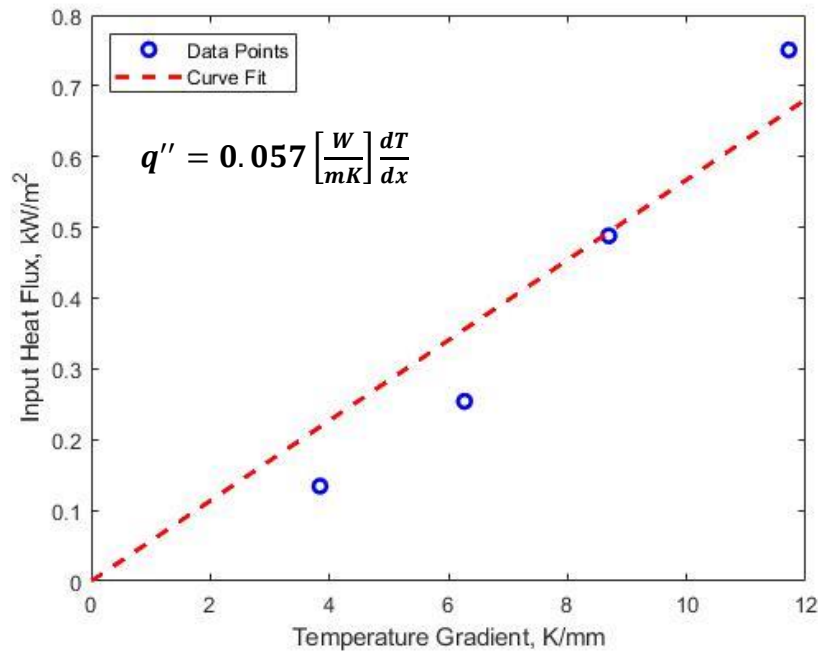


Figure 3.8. Heat flux through the sample in the *uncompressed* state as a function of the sample temperature gradient near the reference-sample interface. The red dashed line shows the best fit (with fixed y-intercept), the slope of which is the effective thermal conductivity of *uncompressed* packing foam using near-interface approximation.

3.3.3 Uncompressed State: One-Dimensional Fin Equation

The exponential like temperature decay observed in the 1-D temperature profile in Figure 3.5 also suggests that when both conduction and convection are present, the foam can be modeled as a fin with prescribed tip temperature. To potentially achieve a more accurate estimate of thermal conductivity, the analysis region selected is only in the center of the foam, as mentioned in section 3.2 and Figure 3.3. This helps to reduce the impact of the horizontal temperature variation (but this variation is considered in the third analysis technique with numerical models).

The normalized temperature profile of a one-dimensional fin model is given by [12]:

$$\frac{\theta}{\theta_b} = \frac{(\theta_L/\theta_b) \sinh mx + \sinh m(L-x)}{\sinh mL}, \text{ where} \quad (3.4)$$

$$m^2 = \frac{hP}{kA_c} \quad (3.5)$$

where P is the equivalent perimeter, A_c is the area of the cross-section of the fin, and L is the total length of the fin or the foam thickness in this case. The difference between the local temperature and ambient temperature is θ , while θ_b is the temperature difference at the base of the fin (the hot side in this case) and θ_L is the temperature difference at the tip of the fin (the cold side in this case).

Figure 3.9 shows the normalized temperature profile along with the best fit temperature profile. The best fit to the temperature data,

$$\frac{\theta}{\theta_b} = \frac{0.2944 \sinh(250.4x) + \sinh[250.4(0.0063-x)]}{\sinh(250.4 \cdot 0.0063)} \quad (3.6)$$

agrees well with the experimental data. The fitted fin parameter m is also shown in Table 3.3. For the power level shown in Figure 3.9, $m = 250$ and the result is consistent between power levels. These consistent results illustrate that the reliability of the fin equation analysis.

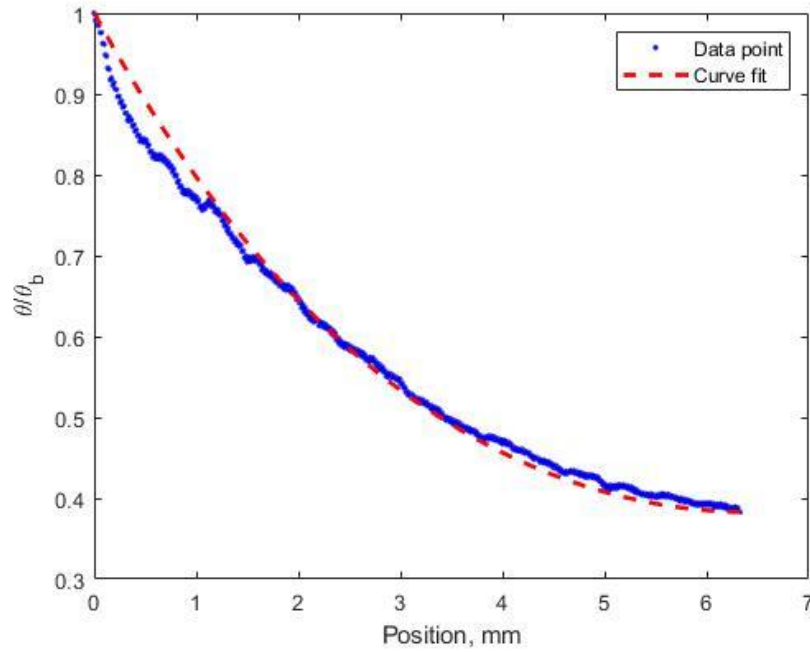


Figure 3.9. Normalized temperature profile obtained from thermal imaging (blue points) compared to the best-fit one-dimensional fin equation (red dashed line).

Table 3.3. Best fit values of the fin parameter m extracted with one-dimensional fin equation.

Temperature Map No.	Curve-fitted m
1	260
2	251
3	250
4	252

The effective convective heat transfer coefficient, h , can be found using Newton's law of cooling by integrating convective heat transfer of all pixels.

$$q_{conv} = q''_{conv}A_c = (q''_{hot} - q''_{cold})A_c = 4h_{eff}(PS)^2 \sum \theta(x, y) \quad (3.7)$$

As the convection heat loss takes place on the sides of the foam, all four surfaces need to be considered. Due to the limitation of the testing instrument, it is assumed that all four surfaces are identical to the top surface. The effective convective heat transfer coefficient is found to be

11.3 W/m²-K. Then, the effective thermal conductivity can be calculated by Equation 3.5 and is found to be 0.071 W/(m-K).

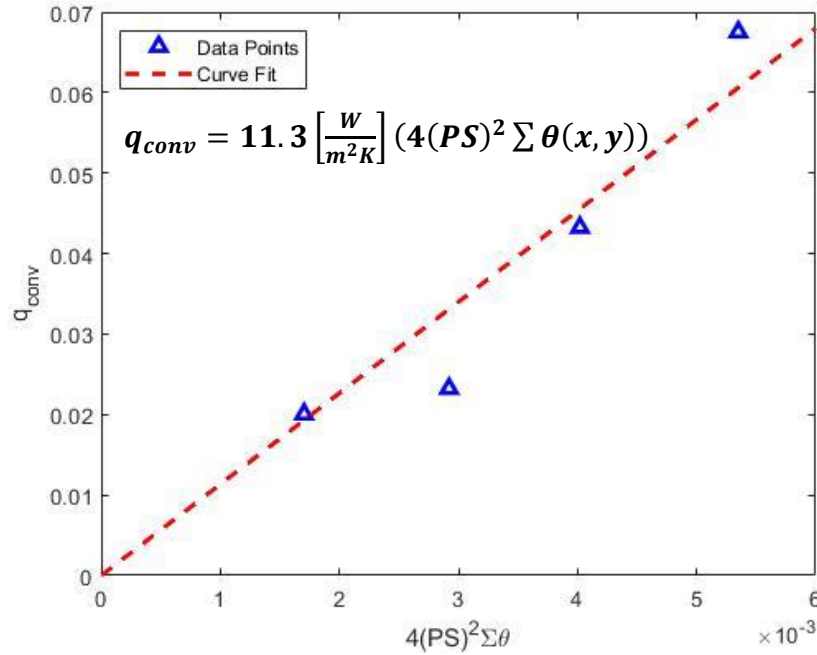


Figure 3.10. Proportional fitting for the derivation of the effective convective heat transfer coefficient of uncompressed packing foam using the fin equation model.

3.3.4 Uncompressed State: 3-D Numerical Simulation

For the highest-fidelity analysis of the foam thermal conductivity, a three-dimensional heat transfer simulation using COMSOL Multiphysics® is conducted, with the goal of confirming the results obtained with the approximate methods.

In COMSOL, the foam is modeled as a rectangular block with four surfaces subjected to convective heat loss. To converge, the simulation setup requires at least one prescribed temperature in the system. In this simulation, this requirement is given by the input of the constant ambient temperature for convection. Thus, the other two surfaces (the square faces that are in contact with the reference layers) are simulated with two sets of boundary conditions. In both cases, the hot side is set to have prescribed inflow heat flux boundary condition, while the cold side is set to have either be the prescribed temperature measured from the IR images or the measured outflow heat flux.

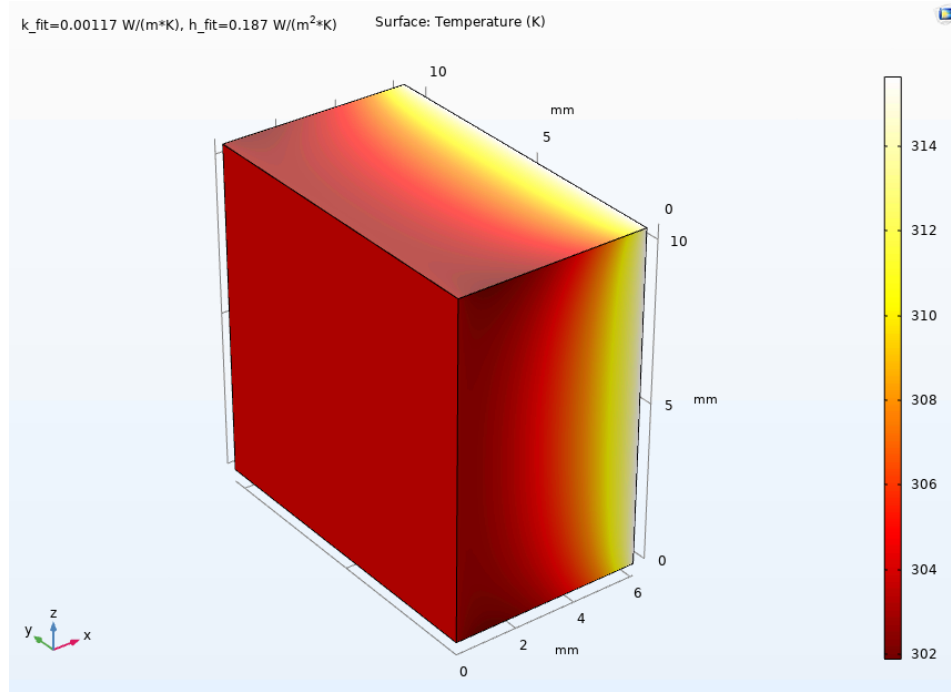


Figure 3.11. Geometry and surface temperature (in K) with a heat transfer coefficient of $h_{eff} = 0.187 \text{ W}/(\text{m}^2\text{K})$ and $k_{eff} = 0.00117 \text{ W}/(\text{m-K})$.

The convective coefficient, h_{eff} , and the thermal conductivity, k_{eff} , are calculated by iterating these values within a reasonable range of values. The simulated temperature map is then compared with the actual temperature map and the mean squared error (MSE) for each set of parameters is computed to determine the best fit. The sample foam region on the original temperature map has a resolution of 500×860 . To reduce the cost of the simulation, the original map is reduced by a factor of 10 to be 50×86 (see Figure 3.12) such that fewer mesh elements can be used. This also smooths the temperature variations observed due to the filamentous nature of the porous foam. The reduced map not only reduces the computing cost, but also the randomness that may cause more chaos in the comparison. Sample simulation outputs are shown in Figure 3.13. The output is extracted from the top surface of the block and is divided into the same resolution to match the reduced experimental temperature map.

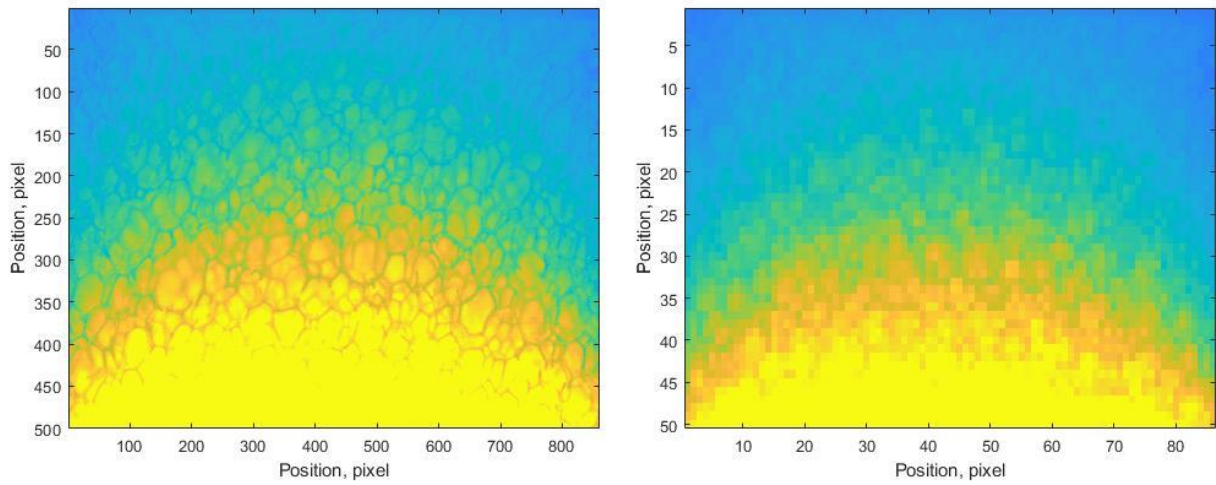


Figure 3.12. Original and reduced temperature map for comparison with the COMSOL Multiphysics® simulation output.

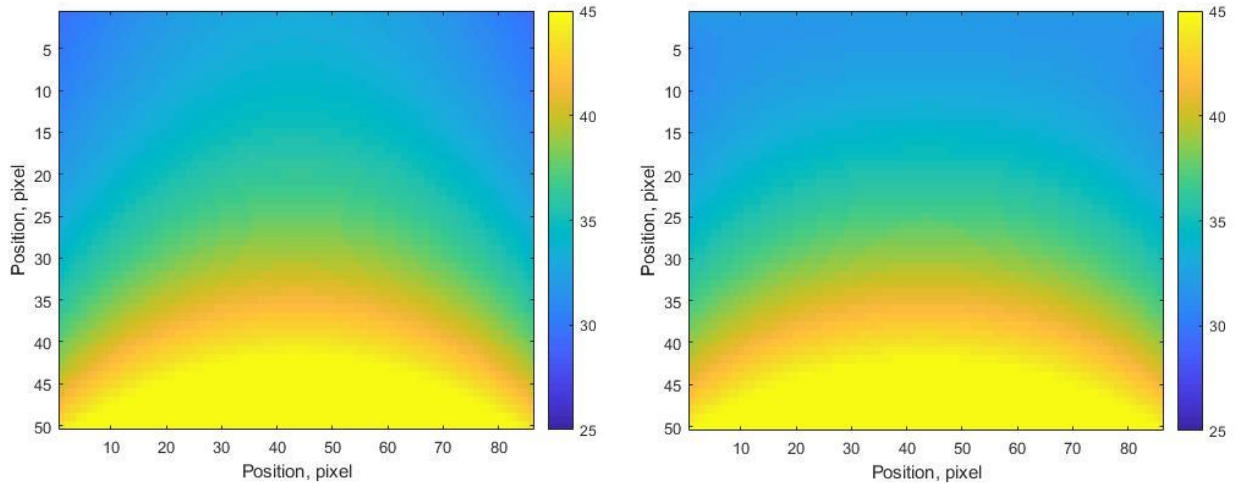


Figure 3.13. Simulated Temperature Maps with two sets of boundary conditions.

Based on the lower fidelity analysis the range of thermal conductivities evaluated are $0.03 - 0.09 \text{ W/(m-K)}$ and the range of heat transfer coefficients are $7 - 13 \text{ W/(m}^2\text{K)}$. Temperature maps are output from COMSOL for pairs of h and k within this range and the mean squared error is computed for each as shown for the case with the prescribed temperature condition on the cold side in Table 3.4 and for the prescribed heat flux on the cold side in Table 3.5. Both boundary conditions yield outputs that have an MSE under 1.0 K^2 for the best fit case.

Table 3.4. Mean Squared Error of Simulated Result with the Prescribed Temperature Boundary Condition on the Cold Side. The best-fit value is bolded and in red text.

		h [W/(m ² K)]						
		13	12	11	10	9	8	7
k [W/(m-K)]	0.09	2.907	1.680	0.980	0.964	1.841	3.881	7.442
	0.08	2.026	1.080	0.797	1.382	3.108	6.336	11.551
	0.07	1.467	0.918	1.213	2.624	5.518	10.386	17.906
	0.06	1.467	1.484	2.592	5.161	9.692	16.876	27.677
	0.05	2.458	3.297	5.576	9.805	16.693	27.233	42.852
	0.04	5.282	7.358	11.383	18.081	28.481	44.070	67.044
	0.03	11.774	15.834	22.618	33.196	49.127	72.735	107.575

Table 3.5. Mean Squared Error of Simulated Result with the Prescribed Heat Flux Boundary Condition on the Cold Side. The best-fit value is bolded and in red text.

		h [W/(m ² K)]						
		14	13	12	11	10	9	8
k [W/(m-K)]	0.10	2.252	1.962	4.292	10.742	23.756	47.461	89.140
	0.09	1.664	1.404	3.769	10.260	23.321	47.081	88.825
	0.08	1.225	1.018	3.445	10.007	23.151	47.007	88.861
	0.07	1.060	0.947	3.481	10.167	23.454	47.476	89.523
	0.06	1.395	1.445	4.168	11.072	24.612	48.927	91.315
	0.05	2.644	2.987	6.049	13.347	27.346	52.198	95.219
	0.04	5.627	6.515	10.213	18.258	33.136	59.031	103.294

The simulations are repeated 3 times and the average values for thermal conductivity and heat transfer coefficient after three rounds of iterations are shown in Table 3.6 along with the values from the lower-fidelity methods for comparison. The results for the extra two rounds of iterations are shown in Appendix A. The data from the COMSOL fitting approach agree well with the 1-D fin approximation for both k_{eff} and h_{eff} .

Table 3.6. Best fit thermal conductivity and convective heat transfer coefficient for the compressed sample with different fitting methods. The resulting MSE is shown for the COMSOL fitting approach.

Foam State	Fitting Approach	k_{eff} [W/(m-K)]	h_{eff} [W/(m ² K)]	MSE
Uncompressed (6.30 mm)	Near Interface	0.057	N/A	N/A
	1-D Fin Approximation	0.071	11.3	N/A
	COMSOL – Fixed Cold Side Temperature	0.080	11.2	0.790
	COMSOL – Fixed Cold Side Heat Flux	0.072	13.4	0.726
Compressed (0.55 mm)	1-D Conduction	0.057	N/A	N/A

3.4 Results Discussion and the Spring Model

The final results of the packing foam are listed in Table 3.6. The effective thermal conductivity of the compressed packing foam is 0.057 W/(m-K). For the uncompressed sample, apart from the near-interface approximation, the other three methods that consider convection losses yield similar results. The effective thermal conductivity of the uncompressed packing foam lies around 0.07-0.08 W/(m-K), which is slightly higher than that of the compressed packing foam. The computed convective heat transfer coefficient is in the range of 11 – 14 W/(m²K). This range agrees with the approximate coefficient for natural convection under room temperature over a surface.

One conclusion that can be made from the experiment is that the effective thermal conductivity of the foam does not increase when the foam is compressed. Instead, the effective thermal conductivity is relatively constant or slightly decreases as the foam is compressed. This result is counter-intuitive as higher density and more branches in contact with compression should enhance heat flow through the sample. Thus, higher thermal conductivity is expected. However, this phenomenon can be explained by analogy to a spring.

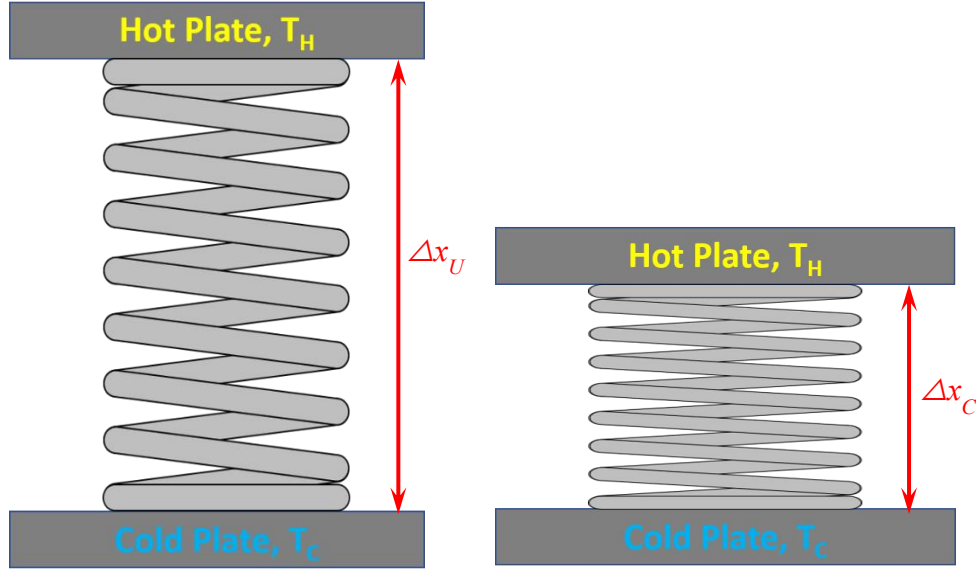


Figure 3.14. Geometry of a spring with compression to explain the unusual thermal conductivity behavior observed for the foams.

Figure 3.14 shows a demonstration of how a spring, which is a one-dimensional compressible media, can achieve similar results as a foam (that are 3D compressible media). The spring is placed between two plates and is compressed. The metal of the spring has a material thermal conductivity of k_m , a total length of L , and a cross-sectional area of A_m . During the compression, the equivalent length of the spring (distance between the plates) is reduced from Δx_1 to Δx_2 . Assuming the cross-sectional area of the spring coil, A_c , is not affected, the effective thermal resistance (inverse of conductance) of the spring in the uncompressed (R_U) and compressed (R_C) states can be written as:

$$R_U = \frac{\Delta x_U}{k_U A_c} = \frac{L}{k_m A_m} \quad (3.8)$$

$$R_C = \frac{\Delta x_C}{k_C A_c} = \frac{L}{k_m A_m} \quad (3.9)$$

For both states, heat flows through the same spring for the same distance. Thus, the effective thermal resistance of the spring is independent to the level of compression:

$$R_{eff} = \frac{\Delta x_U}{k_U A_c} = \frac{\Delta x_C}{k_C A_c}. \quad (3.10)$$

Thus, we can find that the ratio of the thermal conductivities is directly related to the ratio of the spring heights (*i.e.*, separation of the two plates):

$$\frac{k_C}{k_U} = \frac{\Delta x_C}{\Delta x_U}. \quad (3.11)$$

For a one-dimensional spring, the effective thermal resistance is proportional to its equivalent length (see Equation 3.10). The result of the spring model provides an unusual insight into the heat transfer performance of compressible foam materials. This simplified model helps explain the decrease in the effective thermal conductivity, but it requires more factors to describe the experimental results in the practical experiment of graphene-polymer foam in Chapter 2.

The real foams have much more complicated geometry and structure than the spring. During compression, increases in the level of contacts between branches will lead to a decrease in its actual path length for heat transfer and then decrease its effective thermal resistance. Considering the impact of the level of contacts between filaments in the foams leads to the following relations:

$$R_U = \frac{\Delta x_U}{k_U A_c} = \frac{L_U}{k_m A_m}, \quad (3.12)$$

$$R_C = \frac{\Delta x_C}{k_C A_c} = \frac{L_C}{k_m A_m}, \quad (3.13)$$

$$\frac{\Delta x_U}{k_U} = \frac{L_U}{L_C} \frac{\Delta x_C}{k_C} = F \cdot \frac{\Delta x_C}{k_C}, \text{ and} \quad (3.14)$$

$$\frac{k_C}{k_U} = F \cdot \frac{\Delta x_C}{\Delta x_U}. \quad (3.15)$$

The thermal resistance factor, F , is added to adapt the spring model to the packing foam experiment. This factor is equivalent to the ratio of the actual heat transfer length. At the uncompressed state, the actual path length, L_U , is at its maximum. At the compressed state, the actual path length, L_C , is approaching the effective thickness of the foam. Thus, the thermal resistance factor, F , has a range of $1 < F < \frac{\Delta x_U}{\Delta x_C}$. Therefore, the addition of the resistance factor can explain the disagreement in the thermal conductivity and thermal resistance analysis.

4. SIMULATION OF COMPRESSIBLE GRAPHENE NANOFOAM

One of the toughest issues with porous media analysis is the complexity and randomness of the structure [19]. While the commercially available foam on the macro-scale may be studied with continuum scale methods, a foam on the nanoscale can be analyzed by using molecular dynamic simulation, which will provide a unique understanding of how the material contents interacting with each other and achieve switchable thermal conductivity/conductance.

4.1 Simulation Method

This simulation was performed in LAMMPS [25]. The compression process was visualized using VMD [26]. To perform the molecular dynamic simulation, Tersoff potential, which is a multi-body potential, is used to describe carbon-carbon interactions [27]. Periodic boundary condition was applied in all three dimensions, which allows simulation on a relatively small system to represent that on the structure on a larger scale. During the compression process, periodic boundary condition is also required.

The system was first relaxed at 300K for atoms to approach equilibrium position using the Nose-Hoover barostat (NPT ensemble). The foam was then compressed in the z-direction at 300 K by decreasing the dimension in the z-direction of the simulation box. The thermostat was achieved in NVT ensemble. After reaching the desired compression level, the foam was relaxed and equilibrated again with an NVT ensemble at 300K. Then, thermal conductivity k of the foam was calculated according to Green-Kubo method [28, 29] in NVE ensemble. The total thermal conductivity at temperature T is calculated as,

$$k = \frac{V}{3k_B T^2} \int_0^\infty \langle \vec{J}(0) \cdot \vec{J}(t) \rangle dt, \quad (4.1)$$

where, V is the volume of the simulation box, k_B is the Boltzmann constant, t is the correlation time with respect to which the heat current autocorrelation function is integrated, and \vec{J} is the heat current which is calculated as:

$$\vec{J} = \frac{1}{V} \left[\sum_i E_i \vec{v}_i + \frac{1}{2} \sum_{i < j} (\vec{F}_{ij} \cdot (\vec{v}_i + \vec{v}_j) \vec{r}_{ij}) \right], \quad (4.2)$$

where, E is the average total energy of each atom in the system, \vec{v} is the velocity of an atom, \vec{F}_{ij} is the force between atom i and atom j , and \vec{r}_{ij} is the distance between two atoms.

In this simulation, the timestep is $\Delta t = 0.5$ fs. The detailed time period used in the simulation process is listed in Table 4.1.

Table 4.1. Graphene Nanofoam Simulation Time Period.

Step	Timestep size (fs)	Number of timesteps	Total time (ps)
1st relaxation	0.5	100,000	50
Compression		100,000	50
2nd relaxation		1,000,000	500
Calculation		500,000	250

In the thermal conductivity calculation period (Step No.4), the heat current autocorrelation function was computed by sampling every 10 timesteps (5 fs) and 1000 sampling points were to be accumulated. An average was taken every 10,000 timesteps over the 500,000-timestep period. This length of period is provided according to the nanofoam model provider [12] (See Appendix B).

4.2 Simulation Process and Results

To better understand how the compression undergoes in nanoscale, the coordinates of the positions of all atoms at each timestep are recorded and visualized in VMD [26], which provides a motion visualization of the entire compression process. Example images showing the uncompressed and compressed states are shown in Figure 4.1.

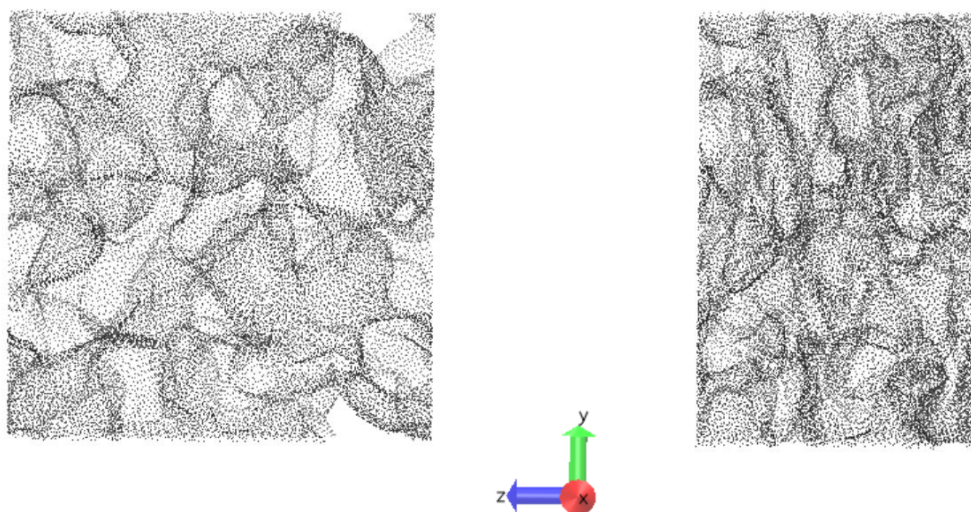


Figure 4.1. The compression process of the graphene nanofoam. (Left) Uncompressed graphene nanofoam after relaxation and, (Right) Compressed graphene nanofoam before relaxation.

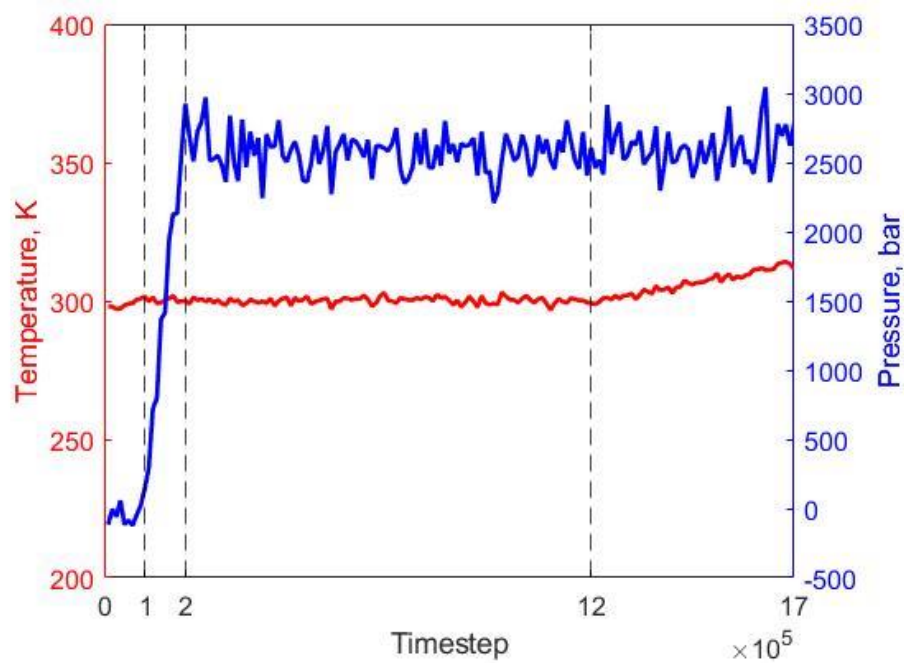


Figure 4.2. Monitoring temperature and pressure changes during a sample trial of the simulation.

The simulation conditions are carefully monitored to ensure reliable results. Temperature and pressure of the system throughout the entire simulation period are recorded in Figure 4.2. These conditions validate the final results of the simulation. The four steps described in Table 4.1 are separated using vertical dash lines. During the initial relaxation step, the pressure of the system is at around 0 to allow the system to equilibrate. Meanwhile, the temperature is set at 300K. In the compression step, the temperature is still set at 300K, while the pressure increases to around 2,700 bar as the foam is being compressed to 75% of its original thickness. In the second relaxation step, the pressure stays constant and the temperature is controlled under the NVT ensemble. In the final calculation step, the pressure stayed around a constant with a fluctuation magnitude of ~500 bars. A small temperature rise is observed, and a possible reason could be the system has not fully reached equilibrium after being compressed. Thus, a part of excess internal energy contributes to the temperature rise. The total increase of temperature is larger for foams with higher density and higher compression percentage since foams that deform in larger scales from their original states are more unstable after compression. The temperature rise could be reduced by extending the second relaxation period after the compression period, in order to stabilize the system before applying Green-Kubo method for thermal conductivity calculation. Since a temperature rise could still be observed, though small in magnitude, it is likely that an even longer relaxation was required for this system. Due to simulation time constrain, the length of 500ps is determined to be the time period for equilibration after compression, though it is not sufficient for a model with high compression percentage or large density. The randomness of the nanofoam structure may also contribute to this long relaxation time requirement.

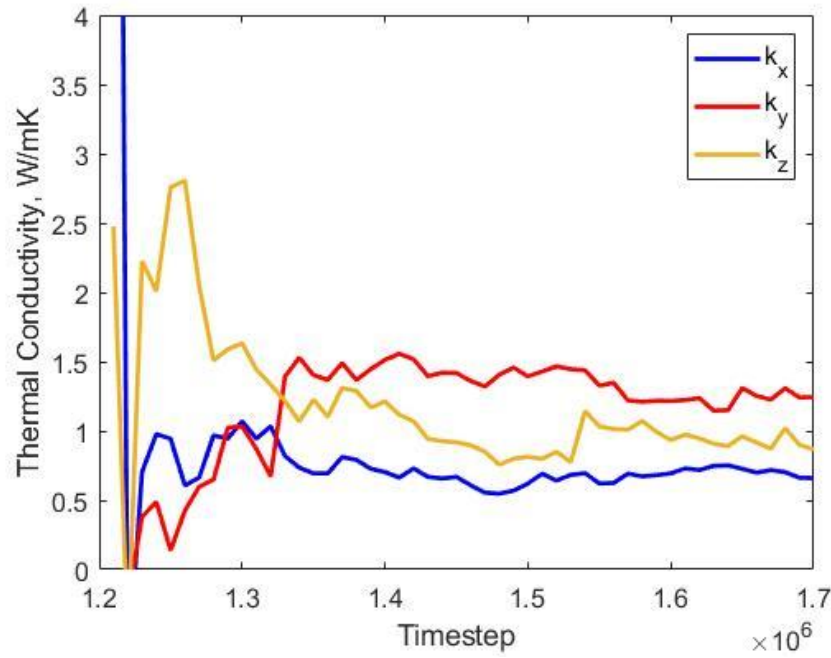


Figure 4.3. Calculated thermal conductivity converges at the end of the simulation.

To ensure that the thermal conductivities obtained at the end of the Green-Kubo calculations are converged and can be accepted as valid results, thermal conductivities in x-, y-, and z-directions over timesteps are shown in Figure 4.3. The results converge rapidly from extreme values during the first 150,000 timesteps. In the next 200,000 timesteps, the results converge and approach final values. And for the last 150,000 timesteps, the data for each direction is fluctuated within a small amount and can be considered as converged. The average thermal conductivity of the system is calculated by taking the average of these three converged values.

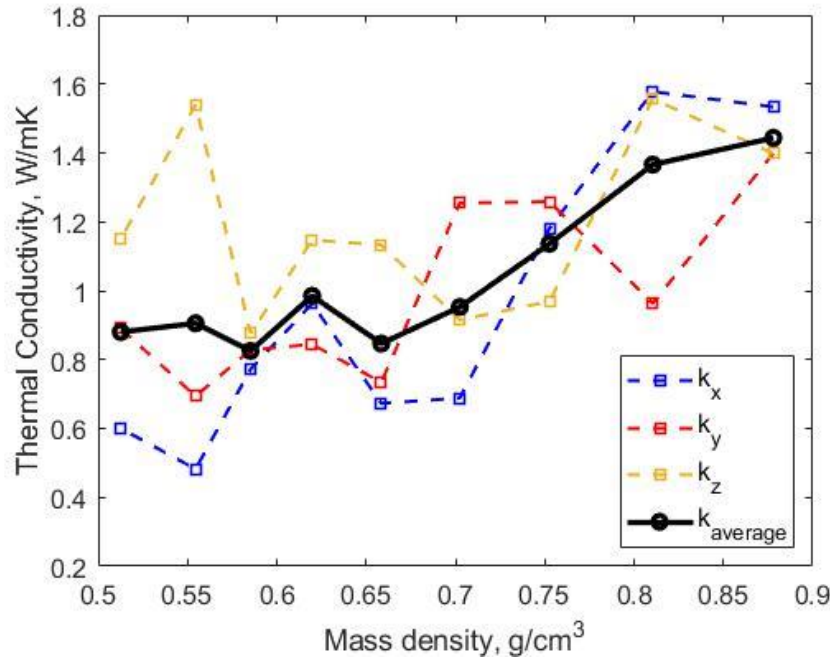


Figure 4.4. Final calculated thermal conductivities of graphene nanofoam by MD simulation.

The calculated thermal conductivities at different compression percentages are shown in Figure 4.4. It can be observed that in general, the total thermal conductivity increases as the system was more compressed. The average thermal conductivity of the system was about 0.90 W/(m-K) at the *uncompressed* state and 1.40 W/(m-K) at the *compressed* state (59% of its original thickness).

4.3 Simulation Outcomes and Discussion

The average thermal conductivity of the system shows an upward trend as it is more compressed, which agrees with the original hypothesis. Thermal conductivities in x- and y-directions also show similar results but have a high level of uncertainties. However, the z-direction thermal conductivity, which is along the compression direction, does not demonstrate clear trends.

There could be several reasons for this. The temperature-rise in Figure 4.2 suggests that the system is not yet in equilibrium, which could cause errors in the relaxed atom positioning. Also, it matches the result obtained in Chapter 3, where we show that thermal conductivity along the compression direction can even decrease if no contacts between the ligaments are established at all. The fact we observe a temperature-insensitive k indicates that a certain level of contact is built during the compression in our modeling.

5. CONCLUSION AND FUTURE WORK

This work has demonstrated the potential of using compressible foam as thermal switching and thermal regulation material. Three aspects regarding the performance and the properties of the compression of foam structures are studied: **(1)** The system testing of the graphene/PDMS foam as the thermal regulator demonstrates a good switching ratio (~ 4), and the reliable and consistent performance from 0 to 30°C. **(2)** The thermal conductivity analysis of a packing foam with compression shows an unusual result with compressed foam exhibiting slightly lower effective thermal conductivity. This result is explained by the spring model, in which the actual heat transfer path length and effective path length are compared. **(3)** The graphene nanofoam simulation shows a tendency to increase its effective thermal conductivity as the nanofoam is compressed. However, the thermal conductivity along the compression direction shows weak dependence on compression, which is consistent with our experimental data on the polymer foams and is bound between the spring limit and other existing theories.

Future works based on these results can be focused on strategies to make the thermal conductivity more sensitive to compression, in order to enhance the switching ratio. Research can be made to obtain better material than the commercially available graphene/PDMS foams to serve as the thermal switching material. Thermal conductivity analysis using the spring model and molecular dynamic simulation can be refined to quantitatively explain the unexpected results. The spring model demonstrated is an ideal one-dimensional case, where more details could be added to analyze real-world applications. Graphene nanofoam simulation in this work still experiences an unstable system temperature. Further improvements could include constructing less dense and more uniform models and creating more stabilized simulation methods.

APPENDIX A. EXTRA ITERATION STEPS IN COMSOL SIMULATION

Table A.1. Second Round of Iteration: Mean Squared Error of Simulated Result with the Prescribed Temperature Boundary Condition on the Cold Side.

		h [(W/m ² K)]						
		11.3	11.2	11.1	11	10.9	10.8	10.7
k [W/(m-K)]	0.083	0.853	0.828	0.811	0.801	0.800	0.806	0.822
	0.082	0.831	0.811	0.798	0.794	0.798	0.811	0.832
	0.081	0.813	0.799	0.792	0.793	0.802	0.821	0.848
	0.080	0.801	0.792	0.790	0.797	0.812	0.837	0.870
	0.079	0.795	0.790	0.794	0.807	0.829	0.859	0.899
	0.078	0.793	0.795	0.804	0.823	0.851	0.888	0.935
	0.077	0.798	0.805	0.821	0.846	0.880	0.924	0.977

Table A.2. Third and Final Round of Iteration: Mean Squared Error of Simulated Result with the Prescribed Temperature Boundary Condition on the Cold Side.

		h [W/(m ² K)]						
		11.30	11.25	11.20	11.15	11.10	11.05	11.00
k [W/(m-K)]	0.0810	0.813	0.805	0.799	0.794	0.792	0.791	0.793
	0.0805	0.807	0.800	0.794	0.791	0.790	0.791	0.794
	0.0800	0.801	0.795	0.792	0.790	0.790	0.792	0.797
	0.0795	0.797	0.793	0.790	0.790	0.791	0.795	0.801
	0.0790	0.795	0.791	0.790	0.791	0.794	0.800	0.807
	0.0785	0.793	0.791	0.792	0.794	0.799	0.805	0.814
	0.0780	0.793	0.793	0.795	0.798	0.804	0.813	0.823

Table A.3. Third and Final Round of Iteration: Mean Squared Error of Simulated Result with the Prescribed Heat Flux Boundary Condition on the Cold Side.

		h [W/(m ² K)]						
		13.6	13.4	13.2	13	12.8	12.6	12.4
k [W/(m-K)]	0.076	0.800	0.757	0.802	0.941	1.184	1.541	2.022
	0.074	0.772	0.733	0.782	0.925	1.172	1.533	2.018
	0.072	0.761	0.726	0.778	0.926	1.178	1.543	2.033
	0.070	0.767	0.737	0.795	0.947	1.204	1.574	2.070
	0.068	0.795	0.770	0.832	0.990	1.252	1.629	2.130
	0.066	0.845	0.826	0.894	1.058	1.327	1.710	2.217
	0.064	0.921	0.908	0.983	1.154	1.430	1.820	2.335

Table A.4. Third and Final Round of Iteration: Mean Squared Error of Simulated Result with the Prescribed Heat Flux Boundary Condition on the Cold Side.

		h [W/(m ² K)]						
		13.55	13.5	13.45	13.4	13.35	13.3	13.25
k [W/(m-K)]	0.0735	0.751	0.738	0.731	0.730	0.734	0.743	0.758
	0.0730	0.747	0.736	0.729	0.728	0.732	0.741	0.757
	0.0725	0.745	0.734	0.727	0.726	0.731	0.740	0.756
	0.0720	0.744	0.733	0.727	0.726	0.731	0.741	0.757
	0.0715	0.744	0.733	0.728	0.727	0.732	0.742	0.759
	0.0710	0.746	0.735	0.729	0.729	0.734	0.745	0.762
	0.0705	0.748	0.738	0.733	0.733	0.738	0.749	0.766

APPENDIX B. GRPAHENE NANOFOAM MODEL

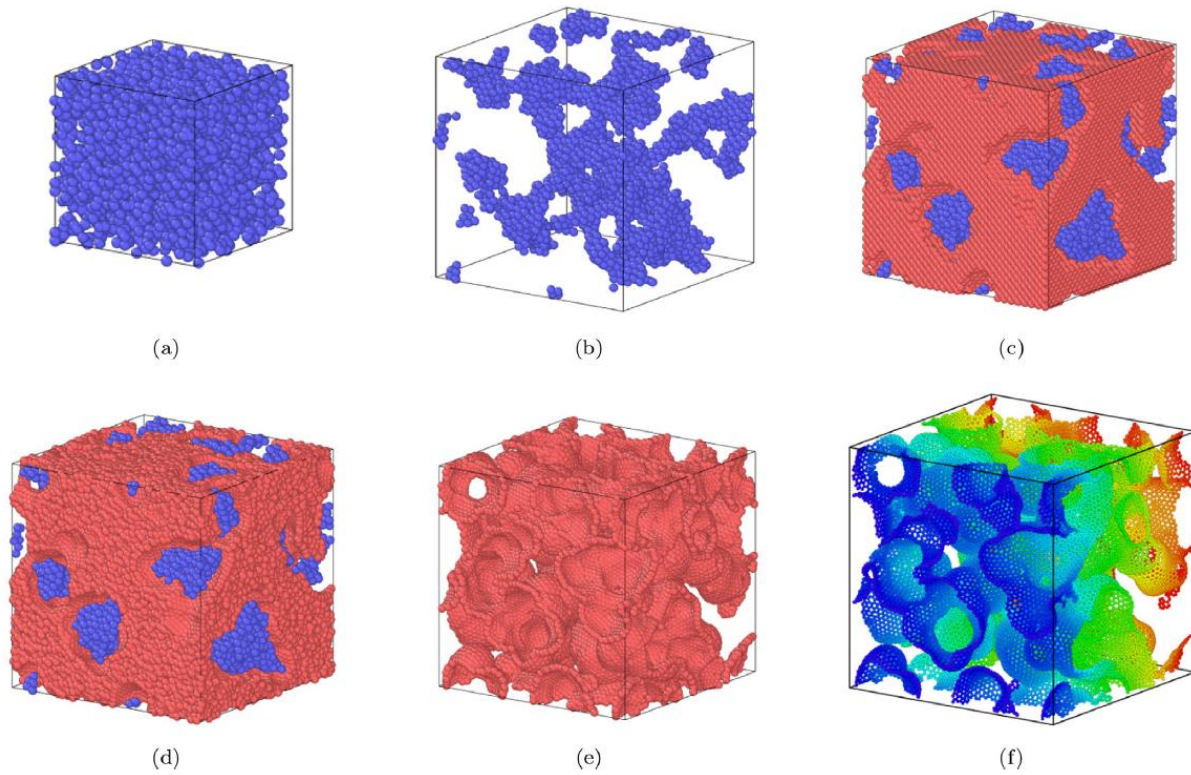


Figure B.1. Construction of Graphene Nanofoam².

The graphene random nanofoam is constructed by A. Pedrielli et al. [11]. **a)** The blue particles are the support particles that are randomly arranged inside the grid. **b)** The grid is expanded to enable optimized support particle positions. **c)** Foam particle (carbon atoms) are inserted on a regular grid basis and those that are too close to supporting particles are removed. **d)** The foam particles are optimized with an attractive potential pulling the two types of particles toward each other by an MD run. **e)** The foam particles are rearranged to be in hexagonal geometry to mimic graphene structure via a Voronoi procedure and the support particles are removed. And **f)** Colored grids to visualize the construction result.

² Figure and construction process from A. Pedrielli et. al, *Carbon*, vol. 132, pp. 766-775, 2018.

REFERENCES

- [1] A. L. Moore and L. Shi, "Emerging challenges and materials for thermal management of electronics," *Materials Today*, vol. 17, no. 4, 2014.
- [2] Y. Liu, Y. Zhu and Y. Cui, "Challenges and opportunities towards fast-charging battery materials," *Nature Energy*, vol. 4, pp. 540-550, 2019.
- [3] M. Rodrigues, G. Babu, H. Gullapalli, K. Kalaga, F. Sayed, K. Kato, J. Joyner and P. Ajayan, "A materials perspective on Li-ion batteries at extreme temperatures," *Nature Energy*, vol. 2, no. 17108, 2017.
- [4] M. Hao, J. Li, S. Park, S. Moura and C. Dames, "Efficient thermal management of Li-ion batteries with a passive interfacial thermal regulator based on a shape memory alloy," *Nature Energy*, vol. 3, pp. 899-906, 2018.
- [5] G. Wehmeyer, T. Yabuki, C. Monachon, J. Wu and C. Dames, "Thermal diodes, regulators, and switches: Physical mechanisms and potential applications," *Applied Physics Reviews*, vol. 4, no. 041304, 2017.
- [6] R. Bywaters and R. Griffin, "A gas-gap thermal switch for cryogenic applications," *Cryogenics*, pp. 345-349, 1973.
- [7] M. Rasekh, S. Khadem and A. Toghrace, "NEMS thermal switch operating based on thermal expansion of carbon nanotubes," *Physica E*, vol. 59, pp. 210-217, 2014.
- [8] Z. Guo, D. Zhang and X. Gong, "Thermal conductivity of graphene nanoribbons," *Applied Physics Letters*, vol. 95, no. 163103, 2009.
- [9] M. Fujii, X. Zhang, H. Xie, H. Ago, K. Takahashi, T. Ikuta, H. Abe and T. Shimizu, "Measuring the Thermal COnductivity of a Single Carbon Nanotube," *Physics Review Letters*, vol. 95, no. 065502, 2005.
- [10] A. Balandin, S. Ghosh, W. Bao, I. Calizo, D. Teweldebrhan, F. Miao and C. Lau, "Superior Thermal Conductivity of Single-Layer Graphene," *Nano Letters*, vol. 8, no. 3, pp. 902-907, 2008.

- [11] A. Pedrielli, S. Taioli, G. Garberoglio and N. Pugno, "Mechanical and thermal properties of graphene random nanofoams via Molecular Dynamics simulations," *Carbon*, vol. 132, pp. 766-775, 2018.
- [12] F. Incropera and D. Dewitt, *Fundamentals of Heat and Mass Transfer*, 7th Edition, John Wiley & Sons, Inc, 2011.
- [13] M. Adams, M. Verosky, M. Zebarjadi and J. Heremans, "High switching ratio variable-temperature solid-state thermal switch based on thermoelectric effects," *International Journal of Heat and Mass Transfer*, vol. 134, pp. 114-118, 2019.
- [14] J. Cho, T. Wiser, C. Richards, D. Bahr and R. Richards, "Fabrication and characterization of a thermal switch," *Sensors and Actuators A*, vol. 133, pp. 55-63, 2007.
- [15] J. Zhu, S. Tang, K. Khoshmanesh and K. Ghorbani, "An integrated liquid cooling system based on Galinstan liquid metal droplets," *Applied Materials & Interfaces*, vol. 8, pp. 2173-2180, 2016.
- [16] S. Jeong, W. Nakayama and S. Lee, "Experimental investigation of a heat switch based on the precise regulation of a liquid bridge," *Applied Thermal Engineering*, vol. 39, pp. 151-156, 2012.
- [17] T. Yang, B. Kwon, P. Weisensee, J. Kang, X. Li, P. Braun, N. Miljkovic and W. King, "Millimeter-scale liquid metal droplet thermal switch," *Applied Physics Letters*, vol. 112, no. 063505, 2018.
- [18] R. Zheng, J. Gao, J. Wang and G. Chen, "Reversible temperature regulation of electrical and thermal conductivity using liquid–solid phase transitions," *Nature Communications*, vol. 2, no. 289, 2011.
- [19] X. Gou, H. Ping, Q. Ou, H. Xiao and S. Qing, "A novel thermoelectric generation system with thermal switch," *Applied Energy*, vol. 160, pp. 843-852, 2015.
- [20] X. Huai, W. Wang and Z. Li, "Analysis of the effective thermal conductivity of fractal porous media," *Applied Thermal Engineering*, vol. 27, pp. 2815-2821, 2007.
- [21] D. Nield, "Estimation of the stagnant thermal conductivity of saturated porous media," *J. Heat Mass Transfer*, vol. 34, no. 6, pp. 1575-1576, 1991.

- [22] M. Kaviany, *Principles of Heat Transfer in Porous Media*, 2nd ed., New York: Springer, 1995.
- [23] C.-W. Nan, R. Birringer, D. Clarke and H. Gleiter, "Effective thermal conductivity of particulate composites with interfacial thermal resistance," *Journal of Applied Physics*, vol. 81, no. 10, pp. 6692-6699, 1997.
- [24] A. Marconnet, N. Yamamoto, M. Panzer, B. Wardle and K. Goodson, "Thermal Conduction in Aligned Carbon Nanotube - Polymer Nanocomposites with High Packing Density," *ACS Nano*, vol. 5, no. 6, pp. 4818-4825, 2011.
- [25] S. Plimpton, "Fast Parallel Algorithms for Short-Range Molecular Dynamics," *Journal of Computational Physics*, vol. 117, no. 1, pp. 1-19, 1995.
- [26] W. Humphrey, A. Dalke and K. Schulten, "VMD: Visual molecular dynamics," *Journal of Molecular Graphics*, vol. 14, no. 1, pp. 33-39, 1996.
- [27] L. Lindsay and D. Broido, "Optimized Tersoff and Brenner empirical potential parameters for lattice dynamics and phonon thermal transport in carbon nanotubes and graphene," *Physical Review B*, vol. 82, no. 209903, 2010.
- [28] M. Green, "Markoff Random Processes and the Statistical Mechanics of Time-Dependent Phenomena. II. Irreversible Processes in Fluids," *Journal of Chemical Physics*, vol. 22, no. 3, 1954.
- [29] R. Kubo, "Statistical-Mechanical Theory of Irreversible Processes. I. General Theory and Simple Applications to Magnetic and Conduction Problems," *Journal of the Physical Society of Japan*, vol. 12, pp. 570-586, 1957.
- [30] X. Ruan and M. Kaviany, "Multiple scattering and nonlinear thermal emission of Yb³⁺, Er³⁺: Y₂O₃ nanopowders," *Journal of Applied Physics*, vol. 95, no. 8, 2004.